



## Methods for calculating stress intensity factors in anisotropic materials: Part I— $z = 0$ is a symmetric plane

Leslie Banks-Sills<sup>a,b,\*</sup>, Itai Hershkovitz<sup>a</sup>, Paul A. Wawrzynek<sup>b</sup>,  
Rami Eliasi<sup>a</sup>, Anthony R. Ingraffea<sup>b</sup>

<sup>a</sup> *The Dreszer Fracture Mechanics Laboratory, Department of Solid Mechanics, Materials and Systems, The Fleischman Faculty of Engineering, Tel Aviv University, 69978 Ramat Aviv, Israel*

<sup>b</sup> *School of Civil and Environmental Engineering, Cornell University, Ithaca, NY 14853, United States*

Received 10 May 2004; received in revised form 17 December 2004; accepted 27 December 2004

Available online 1 July 2005

---

### Abstract

The problem of a crack in general anisotropic material under LEFM conditions is presented. In Part I, three methods are presented for calculating stress intensity factors for various anisotropic materials in which  $z = 0$  is a plane of symmetry. All of the methods employ the displacement field obtained by means of the finite element method. The first one is known as displacement extrapolation and requires the values of the crack face displacements. The other two are conservative integrals based upon the  $J$ -integral. One employs symmetric and asymmetric fields to separate the mode I and II stress intensity factors. The second is the  $M$ -integral which also allows for calculation of  $K_I$  and  $K_{II}$  separately.

All of these methods were originally presented for isotropic materials. Displacement extrapolation and the  $M$ -integral are extended for orthotropic and monoclinic materials, whereas the  $J_I$ - and  $J_{II}$ -integrals are only extended for orthotropic material in which the crack and material directions coincide. Results are obtained by these methods for several problems appearing in the literature. Good to excellent agreement is found in comparison to published values. New results are obtained for several problems.

In Part II, the  $M$ -integral is extended for more general anisotropies. In these cases, three-dimensional problems must be solved, requiring a three-dimensional  $M$ -integral.

© 2005 Elsevier Ltd. All rights reserved.

*Keywords:* Stress intensity factors; Anisotropic material; Finite element method; Conservative integrals

---

\* Corresponding author. Address: The Dreszer Fracture Mechanics Laboratory, Department of Solid Mechanics, Materials and Systems, The Fleischman Faculty of Engineering, Tel Aviv University, 69978 Ramat Aviv, Israel. Tel.: +972 36408132; fax: +972 36407617.

*E-mail addresses:* [banks@eng.tau.ac.il](mailto:banks@eng.tau.ac.il) (L. Banks-Sills), [hersh@eng.tau.ac.il](mailto:hersh@eng.tau.ac.il) (I. Hershkovitz), [wash@fac.cornell.edu](mailto:wash@fac.cornell.edu) (P.A. Wawrzynek), [eliasi@eng.tau.ac.il](mailto:eliasi@eng.tau.ac.il) (R. Eliasi), [aril@cornell.edu](mailto:aril@cornell.edu) (A.R. Ingraffea).

## 1. Introduction

Anisotropic materials are found in many structures, including jet engine turbine blades, in MEMS and NEMS. In those cases, they appear as homogeneous materials. Many composite materials are also anisotropic, although they are inhomogeneous. The propagation of cracks is governed by different laws for each of these material types. But in each case, determination of the stress intensity factors where applicable is similar.

The first paper to deal with cracks in anisotropic material is that of Sih et al. [13]. In that study, the first term in the asymptotic expansion of the stress and displacement fields was determined for a crack in a monoclinic material with  $z = 0$  a plane of symmetry and the crack front perpendicular to this plane. The energy release rate was also given. The next analytical breakthrough was that of Hoenig [7] in which the three-dimensional problem of a through crack in a general anisotropic material was treated.

Numerical studies followed. Stress intensity factors for cracks in orthotropic materials in which  $z = 0$  is a symmetry plane were considered by Atluri et al. [1], Boone et al. [5] and Tohgo et al. [17]. In those studies, the crack may be aligned with the material axes or rotated with respect to them. Atluri et al. [1] employed hybrid finite elements with a square root singularity surrounding the crack tip and regular elements in the rest of the domain to determine stress intensity factors. Boone et al. [5] used quarter point, triangular, singular elements surrounding the crack tip. Displacement correlation was employed to determine stress intensity factors. Several crack propagation theories were described with one used to predict propagation in orthotropic materials. In testing cracked composite specimens, Tohgo et al. [17] obtained stress intensity factors in two ways. Firstly, they used the separated  $J$ -integral method of Ishikawa et al. [8] to obtain the stress intensity factors  $K_I$  and  $K_{II}$ . In their study, the crack and fiber directions coincided. For particular cases, it is shown in our investigation that the separation method is, in fact, valid. Most likely it is valid for the cases they studied. In addition, they calculated the  $J$ -integral and found the ratio of the normal to shear stress ahead of the crack tip by extrapolation. These two conditions are sufficient to produce the two stress intensity factors. It may be noted that differences of 5% were found between the two methods.

In the first part of this investigation, the two-dimensional problem of a crack in monoclinic, orthotropic and cubic materials is considered. The crack is assumed to be along the  $x$ -axis as shown in Fig. 1. In the second part of this study, the more general anisotropic three-dimensional problem of a through crack is examined. Here we begin with the general solution and then specialize it for the case of interest.

The asymptotic stress and displacement fields in the vicinity of the crack tip in a general anisotropic material are presented. These were derived by Hoenig [7] based on the Lekhnitskii [9] formalism. They are given by

$$\sigma_{xx} = \frac{1}{\sqrt{2\pi r}} \Re \left[ \sum_{i=1}^3 \frac{P_i^2 N_{ij}^{-1} K_j}{Q_i} \right], \quad (1)$$

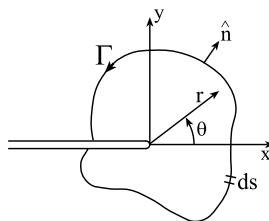


Fig. 1. Path of  $J$ -integral and crack tip coordinates.

$$\sigma_{yy} = \frac{1}{\sqrt{2\pi r}} \Re \left[ \sum_{i=1}^3 \frac{N_{ij}^{-1} K_j}{Q_i} \right], \quad (2)$$

$$\sigma_{xy} = -\frac{1}{\sqrt{2\pi r}} \Re \left[ \sum_{i=1}^3 \frac{p_i N_{ij}^{-1} K_j}{Q_i} \right], \quad (3)$$

$$\sigma_{zx} = \frac{1}{\sqrt{2\pi r}} \Re \left[ \sum_{i=1}^3 \frac{p_i \lambda_i N_{ij}^{-1} K_j}{Q_i} \right], \quad (4)$$

$$\sigma_{zy} = -\frac{1}{\sqrt{2\pi r}} \Re \left[ \sum_{i=1}^3 \frac{\lambda_i N_{ij}^{-1} K_j}{Q_i} \right], \quad (5)$$

$$u_i = \sqrt{\frac{2r}{\pi}} \Re \left[ \sum_{j=1}^3 m_{ij} N_{jl}^{-1} K_l Q_j \right], \quad (6)$$

where  $\Re$  represents the real part of the quantity in brackets, two repeated indices in (1)–(6) obey the summation convention from 1 to 3, the coordinates  $x$ ,  $y$ ,  $z$ ,  $r$  and  $\theta$  refer to the crack coordinates in Fig. 1,  $K_j$  are the stress intensity factors  $K_I$ ,  $K_{II}$  and  $K_{III}$ . It is assumed that the stresses and displacements are functions only of the in-plane coordinates. Before defining  $p_i$ ,  $\lambda_i$ ,  $m_{ij}$ ,  $N_{ij}$ , and  $Q_i$ , the compliance matrix  $s_{ij}$  must be rotated to the crack tip coordinates. In order that the notation will be clear, the rotated matrix is defined as  $S_{ij}$  where  $i$  and  $j$  take on values 1 through 6; these refer to the crack tip or problem coordinates and not the material coordinates. Note that the compliance matrix is given in contracted notation as  $S_{ij}$ ; the indices are taken such that  $23 \rightarrow 4$ ,  $13 \rightarrow 5$  and  $12 \rightarrow 6$ . The material coordinates are taken as  $x_1$ ,  $x_2$  and  $x_3$  and are in directions arbitrary to the problem or crack coordinates.

For plane stress conditions, the full matrix is employed. For a plane strain problem, the reduced compliance matrix is obtained from

$$S'_{ij} = S_{ij} - \frac{S_{i3}S_{3j}}{S_{33}}, \quad (7)$$

where  $i, j = 1, 2, 4, 5, 6$ ,  $S'_{ij}$  is symmetric and

$$S'_{i3} = S'_{3i} = 0. \quad (8)$$

The parameters  $p_i$ ,  $i = 1, 2, 3$ , are the eigenvalues of the compatibility equations with positive imaginary part. These are found, in general, from the characteristic sixth order polynomial equation

$$l_4(p)l_2(p) - l_3^2(p) = 0, \quad (9)$$

where

$$l_2(p) = S'_{55}p^2 - 2S'_{45}p + S'_{44}, \quad (10)$$

$$l_3(p) = S'_{15}p^3 - (S'_{14} + S'_{56})p^2 + (S'_{25} + S'_{46})p - S'_{24}, \quad (11)$$

$$l_4(p) = S'_{11}p^4 - 2S'_{16}p^3 + (2S'_{12} + S'_{66})p^2 - 2S'_{26}p + S'_{22}. \quad (12)$$

Solution of (9) leads to three pairs of complex conjugate roots. As mentioned previously, the three with positive imaginary part are chosen in Eqs. (1)–(6). The reduced compliance coefficients in (10)–(12) may be replaced by the ordinary compliances for plane stress. The parameters  $\lambda_i$  are given by

$$\lambda_i = -\frac{l_3(p_i)}{l_2(p_i)}, \quad (13)$$

where  $i = 1, 2, 3$ . The parameters  $m_{ij}$  are given by

$$m_{1i} = S'_{11}p_i^2 - S'_{16}p_i + S'_{12} + \lambda_i(S'_{15}p_i - S'_{14}), \tag{14}$$

$$m_{2i} = S'_{21}p_i - S'_{26} + S'_{22}/p_i + \lambda_i(S'_{25} - S'_{24}/p_i), \tag{15}$$

$$m_{3i} = S'_{41}p_i - S'_{46} + S'_{42}/p_i + \lambda_i(S'_{45} - S'_{44}/p_i). \tag{16}$$

The expressions in (13)–(16) appear to rely on the Lekhnitskii formalism [9], although there are differences with Lekhnitskii for  $\lambda_3$  and  $m_{3i}$ . The expressions developed by Hoenig [7] are correct.

The matrix

$$N_{ij} = \begin{pmatrix} 1 & 1 & 1 \\ -p_1 & -p_2 & -p_3 \\ -\lambda_1 & -\lambda_2 & -\lambda_3 \end{pmatrix}; \tag{17}$$

its inverse is given by

$$N_{ij}^{-1} = \frac{1}{|N|} \begin{pmatrix} p_2\lambda_3 - p_3\lambda_2 & \lambda_3 - \lambda_2 & p_2 - p_3 \\ p_3\lambda_1 - p_1\lambda_3 & \lambda_1 - \lambda_3 & p_3 - p_1 \\ p_1\lambda_2 - p_2\lambda_1 & \lambda_2 - \lambda_1 & p_1 - p_2 \end{pmatrix} \tag{18}$$

and  $|N|$  is the determinant of the matrix  $N_{ij}$ . Finally,

$$Q_i = \sqrt{\cos \theta + p_i \sin \theta}. \tag{19}$$

There are special anisotropies for which the above development is mathematically degenerate. These include monoclinic materials with  $x_3 = z = 0$  being a symmetry plane, as well as orthotropic and cubic materials for which all three material axes are perpendicular to symmetry planes and  $x_3 = z = 0$  is a symmetry plane. The stress and displacement fields for the degenerate cases are given in [7,13]. The forms of the expressions presented in these two papers differ, but they agree.

If the material is monoclinic with  $x_3 = z = 0$  a plane of symmetry, then

$$S'_{14} = S'_{24} = S'_{15} = S'_{25} = S'_{46} = S'_{56} = 0. \tag{20}$$

This implies that  $I_3 = 0$  in (11) and  $\lambda_i = 0$  in Eq. (13). The values of  $m_{ij}$  in (14)–(16) become

$$m_{1i} = S'_{11}p_i^2 - S'_{16}p_i + S'_{12}, \tag{21}$$

$$m_{2i} = S'_{21}p_i - S'_{26} + S'_{22}/p_i, \tag{22}$$

$$m_{3i} = 0 \tag{23}$$

for  $i = 1, 2$  and

$$m_{13} = m_{23} = 0, \tag{24}$$

$$m_{33} = S'_{45} - S'_{44}/p_3. \tag{25}$$

Following Hoenig [7], the stress and displacement fields in the neighborhood of the crack tip are given by

$$\sigma_{xx} = \frac{1}{\sqrt{2\pi r}} \Re \left[ \sum_{i=1}^2 \frac{p_i^2 B_i}{Q_i} \right], \tag{26}$$

$$\sigma_{yy} = \frac{1}{\sqrt{2\pi r}} \Re \left[ \sum_{i=1}^2 \frac{B_i}{Q_i} \right], \tag{27}$$

$$\sigma_{xy} = -\frac{1}{\sqrt{2\pi r}} \Re \left[ \sum_{i=1}^2 \frac{p_i B_i}{Q_i} \right], \quad (28)$$

$$\sigma_{zx} = \frac{1}{\sqrt{2\pi r}} \Re \left[ \frac{p_3 B_3}{Q_3} \right], \quad (29)$$

$$\sigma_{zy} = -\frac{1}{\sqrt{2\pi r}} \Re \left[ \frac{B_3}{Q_3} \right], \quad (30)$$

$$u_i = \sqrt{\frac{2r}{\pi}} \Re \left[ \sum_{j=1}^3 m_{ij} B_j Q_j \right], \quad (31)$$

where

$$\begin{pmatrix} B_1 \\ B_2 \\ B_3 \end{pmatrix} = \frac{1}{p_2 - p_1} \begin{pmatrix} p_2 & 1 & 0 \\ -p_1 & -1 & 0 \\ 0 & 0 & p_1 - p_2 \end{pmatrix} \begin{pmatrix} K_I \\ K_{II} \\ K_{III} \end{pmatrix}. \quad (32)$$

It may be noted that most expressions for mode III deformation are presented in this part of the investigation, although no numerical results are obtained.

For an orthotropic material with symmetry planes  $x_i = 0$  ( $i = 1, 2, 3$ ) and with coincident material and crack coordinates, one finds, in addition to (20),

$$S'_{16} = S'_{26} = S'_{45} = 0. \quad (33)$$

As with the monoclinic material,  $l_3 = 0$  in Eq. (11) and thus  $\lambda_i = 0$  in Eq. (13). The values of  $m_{ij}$  in (14)–(16) are now given by

$$m_{1i} = S'_{11} p_i^2 + S'_{12} \quad (34)$$

$$m_{2i} = S'_{21} p_i + S'_{22}/p_i \quad (35)$$

$$m_{3i} = 0 \quad (36)$$

for  $i = 1, 2$  and

$$m_{13} = m_{23} = 0 \quad (37)$$

$$m_{33} = -S'_{44}/p_3. \quad (38)$$

The asymptotic stress and displacement fields presented above were employed by Hoenig [7] to obtain relationships between the  $J$ -integral and stress intensity factors. These are described in Section 2. In Section 3, three methods for calculating stress intensity factors are discussed for the special case of a monoclinic material with  $x_3 = z = 0$  a plane of symmetry. These methods are employed for several problems in the literature and presented in Section 4. Solutions to several new problems are also described. In Part II of this study, a through crack in which the material and crack coordinates do not coincide is treated.

## 2. Relationship between the $J$ -integral and the stress intensity factors

The  $J$ -integral developed by Rice [12] is given by

$$J = \int_{\Gamma} \left( W n_x - T_i \frac{\partial u_i}{\partial x} \right) ds, \quad (39)$$

where the integration path  $\Gamma$  is illustrated in Fig. 1, the strain energy density

$$W = \frac{1}{2} \sigma_{ij} \epsilon_{ij}, \tag{40}$$

the outer normal to  $\Gamma$  is  $n_i$ , the traction vector is  $T_i = \sigma_{ij} n_j$ ,  $u_i$  is the displacement vector and  $ds$  is differential arc length along  $\Gamma$ . Note that the  $J$ -integral is written in terms of crack tip coordinates.

By means of the crack closure integral, Hoengig [7] developed the relationship between the  $J$ -integral and the stress intensity factors as

$$J = -\frac{1}{2} \left\{ K_I \Im(m_{2i} N_{ij}^{-1} K_j) + K_{II} \Im(m_{1i} N_{ij}^{-1} K_j) + K_{III} \Im(m_{3i} N_{ij}^{-1} K_j) \right\}, \tag{41}$$

where  $\Im$  represents the imaginary part of the expression in parentheses and summation should be applied to repeated indices.

For monoclinic materials in which  $x_3 = z = 0$  is a symmetry plane, Eq. (41) reduces to

$$J = \frac{1}{2} \Im \left\{ -\left( \frac{p_1 + p_2}{p_1 p_2} \right) S'_{22} K_I^2 + \left[ S'_{11} p_1 p_2 - \frac{S'_{22}}{p_1 p_2} \right] K_I K_{II} + (p_1 + p_2) S'_{11} K_{II}^2 \right\} + \frac{1}{2} \sqrt{S'_{44} S'_{55} - S'^2_{45}} K_{III}^2. \tag{42}$$

The in-plane terms in (42) agree with those presented in [13]; the mode III term may be shown to agree with that given in a later study of Sih and Liebowitz [14].

If the material is orthotropic with material and crack coordinates coinciding, the expression in Eq. (42) reduces to

$$J = \frac{D_o}{2} \left[ \sqrt{S'_{22} K_I^2} + \sqrt{S'_{11} K_{II}^2} \right] + \frac{1}{2} \sqrt{S'_{44} S'_{55} - S'^2_{45}} K_{III}^2, \tag{43}$$

where

$$D_o = \left[ 2\sqrt{S'_{11} S'_{22}} + 2S'_{12} + S'_{66} \right]^{1/2}. \tag{44}$$

### 3. Methods for calculating stress intensity factors

In this section, several methods are presented for calculating stress intensity factors when  $x_3 = z = 0$  is a symmetry plane. First, the  $M$ -integral is presented for monoclinic and orthotropic material. The conservative  $M$ -integral was first presented by Yau et al. [20] for mixed mode problems in isotropic material and then by Wang et al. [18] for monoclinic and orthotropic material. Next, the displacement extrapolation method is extended for these cases. Finally, the  $J$ -integral is separated into components  $J_I$  and  $J_{II}$  for orthotropic material when the material and crack coordinates coincide. This follows closely the derivation of Ishikawa et al. [8] for isotropic material. In Part II of this study, the  $M$ -integral is extended to three dimensions and general anisotropic material is treated.

#### 3.1. The $M$ -integral

In this section, the conservative  $M$ -integral is extended for monoclinic and orthotropic material when  $x_3 = z = 0$  is a symmetry plane. With the  $J$ -integral in Eq. (39) and the relation in Eq. (42), the combination of the stress intensity factors may be calculated for monoclinic materials. The  $M$ -integral may be employed to determine the individual stress intensity factors. To obtain the  $M$ -integral from (42), two solutions are assumed and superposed; this is possible since the material is linearly elastic. Thus, define

$$\sigma_{ij} = \sigma_{ij}^{(1)} + \sigma_{ij}^{(2)}, \quad (45)$$

$$\epsilon_{ij} = \epsilon_{ij}^{(1)} + \epsilon_{ij}^{(2)}, \quad (46)$$

$$u_i = u_i^{(1)} + u_i^{(2)}. \quad (47)$$

The stress intensity factors associated with the superposed solutions are

$$K_I = K_I^{(1)} + K_I^{(2)}, \quad (48)$$

$$K_{II} = K_{II}^{(1)} + K_{II}^{(2)}, \quad (49)$$

$$K_{III} = K_{III}^{(1)} + K_{III}^{(2)}. \quad (50)$$

On the one hand, the stress, strain and displacement fields are substituted into the expression for the  $J$ -integral in (39). This leads to

$$J = J^{(1)} + J^{(2)} + M^{(1,2)}, \quad (51)$$

where

$$J^{(1)} = \int_{\Gamma} \left( W^{(1)} n_1 - T_i^{(1)} \frac{\partial u_i^{(1)}}{\partial x_1} \right) ds, \quad (52)$$

$$J^{(2)} = \int_{\Gamma} \left( W^{(2)} n_1 - T_i^{(2)} \frac{\partial u_i^{(2)}}{\partial x_1} \right) ds, \quad (53)$$

$$M^{(1,2)} = \int_{\Gamma} \left( W^{(1,2)} n_1 - T_i^{(1)} \frac{\partial u_i^{(2)}}{\partial x_1} - T_i^{(2)} \frac{\partial u_i^{(1)}}{\partial x_1} \right) ds. \quad (54)$$

The superscripts (1) and (2) in (52)–(54) refer to solutions (1) and (2), respectively. The interaction strain energy density is given by

$$W^{(1,2)} = \sigma_{ij}^{(1)} \epsilon_{ij}^{(2)} = \sigma_{ij}^{(2)} \epsilon_{ij}^{(1)} \quad (55)$$

and  $M^{(1,2)}$  is the  $M$ -integral.

On the other hand, the superposed stress intensity factors in (48)–(50) are substituted into (42) to yield

$$\begin{aligned} J = J^{(1)} + J^{(2)} - \mathfrak{I} \left( \frac{p_1 + p_2}{p_1 p_2} \right) S'_{22} K_I^{(1)} K_I^{(2)} + \frac{1}{2} \mathfrak{I} \left( p_1 p_2 S'_{11} - \frac{S'_{22}}{p_1 p_2} \right) \left[ K_I^{(1)} K_{II}^{(2)} + K_I^{(2)} K_{II}^{(1)} \right] \\ + \mathfrak{I} (p_1 + p_2) S'_{11} K_{II}^{(1)} K_{II}^{(2)} + \sqrt{S'_{44} S'_{55} - S'^2_{45}} K_{III}^{(1)} K_{III}^{(2)}, \end{aligned} \quad (56)$$

where

$$\begin{aligned} J^{(1)} = \frac{1}{2} \mathfrak{I} \left\{ - \left( \frac{p_1 + p_2}{p_1 p_2} \right) S'_{22} K_I^{(1)2} + \left[ S'_{11} p_1 p_2 - \frac{S'_{22}}{p_1 p_2} \right] K_I^{(1)} K_{II}^{(1)} + (p_1 + p_2) S'_{11} K_{II}^{(1)2} \right\} \\ + \frac{1}{2} \sqrt{S'_{44} S'_{55} - S'^2_{45}} K_{III}^{(1)2} \end{aligned} \quad (57)$$

and

$$\begin{aligned} J^{(2)} = \frac{1}{2} \mathfrak{I} \left\{ - \left( \frac{p_1 + p_2}{p_1 p_2} \right) S'_{22} K_I^{(2)2} + \left[ S'_{11} p_1 p_2 - \frac{S'_{22}}{p_1 p_2} \right] K_I^{(2)} K_{II}^{(2)} + (p_1 + p_2) S'_{11} K_{II}^{(2)2} \right\} \\ + \frac{1}{2} \sqrt{S'_{44} S'_{55} - S'^2_{45}} K_{III}^{(2)2}. \end{aligned} \quad (58)$$

Equating (51) and (56), leads to the definition of the  $M$ -integral as

$$M^{(1,2)} = -\mathfrak{I} \left( \frac{p_1 + p_2}{p_1 p_2} \right) S'_{22} K_I^{(1)} K_I^{(2)} + \frac{1}{2} \mathfrak{I} \left( p_1 p_2 S'_{11} - \frac{S'_{22}}{p_1 p_2} \right) \left[ K_I^{(1)} K_{II}^{(2)} + K_I^{(2)} K_{II}^{(1)} \right] + \mathfrak{I} (p_1 + p_2) S'_{11} K_{II}^{(1)} K_{II}^{(2)} + \sqrt{S'_{44} S'_{55} - S'^2_{45}} K_{III}^{(1)} K_{III}^{(2)}. \tag{59}$$

Before considering implementation of the  $M$ -integral, its expression in (54) which is a line integral is converted into an area integral following Li et al. [10]. It is well known that area integrals lead to more accurate, stable results than line integrals (see [3]). By defining a function  $q_1$  which is zero on  $C_2$ , unity on  $C_1$  and differentiable within  $A$  (see Fig. 2), it is possible to convert the  $M$ -integral in (54) into an area integral as

$$M^{(1,2)} = \int_A \left( \sigma_{ij}^{(1)} \frac{\partial u_i^{(2)}}{\partial x_j} + \sigma_{ij}^{(2)} \frac{\partial u_i^{(1)}}{\partial x_j} - W^{(1,2)} \delta_{1j} \right) \frac{\partial q_1}{\partial x_j} ds, \tag{60}$$

where  $\delta_{ij}$  is the Kronecker delta.

The function  $q_1$  is defined for eight noded isoparametric elements as

$$q_1 = \sum_{m=1}^8 N_m(\xi, \eta) q_{1m}, \tag{61}$$

where  $N_m$  are the finite element shape functions and  $\xi$  and  $\eta$  are the coordinates of the parent element (for further details, see [4]). Calculation of the  $M$ -integral is carried out in a ring of elements surrounding the crack tip (area  $A$  in Fig. 2, for example). The elements within the ring move as a rigid body. For each of these elements  $q_1$  is unity; so that, the derivative of  $q_1$  with respect to  $x_j$  is zero. For all elements outside the ring,  $q_1$  is zero; so that, again the derivative of  $q_1$  is zero. For elements belonging to the ring, the vector  $q_{1m}$  in (61) is chosen so that the virtual crack extension does not disturb the relative nodal point positions in their new locations; for example, a regular element with nodes at the mid-sides contains only mid-side nodes after distortion.

In order to implement the  $M$ -integral numerically, two solutions are chosen. Solution (1) is the finite element solution of the problem to be solved. Solution (2) is an auxiliary solution. Three auxiliary solutions are chosen here in order to obtain  $K_I^{(1)}$ ,  $K_{II}^{(1)}$  and  $K_{III}^{(1)}$ ; these are denoted as (2a), (2b) and (2c), respectively.

For solution (2a), choose  $K_I^{(2a)} = 1$  and  $K_{II}^{(2a)} = K_{III}^{(2a)} = 0$ . In this case, Eq. (59) becomes

$$M^{(1,2a)} = -\mathfrak{I} \left( \frac{p_1 + p_2}{p_1 p_2} \right) S'_{22} K_I^{(1)} + \frac{1}{2} \mathfrak{I} \left( p_1 p_2 S'_{11} - \frac{S'_{22}}{p_1 p_2} \right) K_{II}^{(1)}. \tag{62}$$

On the other hand, from Eq. (60)

$$M^{(1,2a)} = \int_A \left( \sigma_{ij}^{(1)} \frac{\partial u_i^{(2a)}}{\partial x_j} + \sigma_{ij}^{(2a)} \frac{\partial u_i^{(1)}}{\partial x_j} - W^{(1,2a)} \delta_{1j} \right) \frac{\partial q_1}{\partial x_j} ds. \tag{63}$$

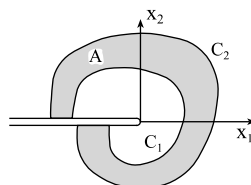


Fig. 2. Path for area  $M$ -integral.

The displacements required for solution (1) are taken from a finite element analysis of the problem to be solved; the stresses and strains are calculated from these. Asymptotic expressions for the stresses, strains and displacements for solution (2a) are given by Eqs. (26)–(28) and (31) with the appropriated stress intensity factor values.

For solution (2b), choose  $K_{II}^{(2b)} = 1$  and  $K_I^{(2b)} = K_{III}^{(2b)} = 0$ . In this case, Eq. (59) becomes

$$M^{(1,2b)} = \frac{1}{2} \mathfrak{I} \left( p_1 p_2 S'_{11} - \frac{S'_{22}}{p_1 p_2} \right) K_I^{(1)} + \mathfrak{I} (p_1 + p_2) S'_{11} K_{II}^{(1)}. \tag{64}$$

On the other hand, from Eq. (60)

$$M^{(1,2b)} = \int_A \left( \sigma_{ij}^{(1)} \frac{\partial u_i^{(2b)}}{\partial x_1} + \sigma_{ij}^{(2b)} \frac{\partial u_i^{(1)}}{\partial x_j} - W^{(1,2b)} \delta_{1j} \right) \frac{\partial q_1}{\partial x_j} ds. \tag{65}$$

Again, the displacements required for solution (1) are taken from a finite element analysis of the problem to be solved; the stresses and strains are calculated from these. Asymptotic expressions for the stresses, strains and displacements for solution (2b) are given by Eqs. (26)–(28) and (31) with the appropriated stress intensity factor values.

Finally, for solution (2c), choose  $K_{III}^{(2c)} = 1$  and  $K_I^{(2c)} = K_{II}^{(2c)} = 0$ . In this case, Eq. (59) becomes

$$M^{(1,2c)} = \sqrt{S'_{44} S'_{55} - S'^2_{45}} K_{III}^{(1)}. \tag{66}$$

On the other hand, from Eq. (60)

$$M^{(1,2c)} = \int_A \left( \sigma_{ij}^{(1)} \frac{\partial u_i^{(2c)}}{\partial x_1} + \sigma_{ij}^{(2c)} \frac{\partial u_i^{(1)}}{\partial x_1} - W^{(1,2c)} \delta_{1j} \right) \frac{\partial q_1}{\partial x_j} ds. \tag{67}$$

Again, the displacements required for solution (1) are taken from a finite element analysis of the problem to be solved; the stresses and strains are calculated from these. Asymptotic expressions for the stresses, strains and displacements for solution (2c) are given by Eqs. (29)–(31) with the appropriated stress intensity factor values.

Since there is a separation between the in-plane and out-of-plane problem, there are two simultaneous linear equations (62) and (64) which may be solved for the unknowns  $K_I^{(1)}$  and  $K_{II}^{(1)}$  as

$$K_I^{(1)} = \frac{2}{D} \left[ -2\mathfrak{I} (p_1 + p_2) S'_{11} M^{(1,2a)} + \mathfrak{I} \left( p_1 p_2 S'_{11} - \frac{S'_{22}}{p_1 p_2} \right) M^{(1,2b)} \right], \tag{68}$$

$$K_{II}^{(1)} = \frac{2}{D} \left[ \mathfrak{I} \left( p_1 p_2 S'_{11} - \frac{S'_{22}}{p_1 p_2} \right) M^{(1,2a)} + 2\mathfrak{I} \left( \frac{p_1 + p_2}{p_1 p_2} \right) S'_{22} M^{(1,2b)} \right], \tag{69}$$

where

$$D = 4\mathfrak{I} (p_1 + p_2) \mathfrak{I} \left( \frac{p_1 + p_2}{p_1 p_2} \right) S'_{11} S'_{22} + \left[ \mathfrak{I} \left( p_1 p_2 S'_{11} - \frac{S'_{22}}{p_1 p_2} \right) \right]^2. \tag{70}$$

The values of  $M^{(1,2a)}$  and  $M^{(1,2b)}$  in (68) and (69) are obtained by evaluating the integrals in (63) and (65). Solving for  $K_{III}^{(1)}$  from Eq. (66) is straightforward.

The  $M$ -integral is considered next, for the case of orthotropic material when the material and problem coordinates coincide. Here, the relation between  $J$  and the stress intensity factors is given in (43). This leads to an expression for  $M^{(1,2)}$  as

$$M^{(1,2)} = D_o \left( \sqrt{S'_{22} K_I^{(1)} K_I^{(2)}} + \sqrt{S'_{11} K_{II}^{(1)} K_{II}^{(2)}} \right) + \sqrt{S'_{44} S'_{55} - S'^2_{45}} K_{III}^{(1)} K_{III}^{(2)}, \tag{71}$$

where  $D_o$  is given in (44).

In this case, there is a separate equation for each stress intensity factor; that is

$$K_I^{(1)} = \frac{1}{D_o \sqrt{S'_{22}}} M^{(1,2a)}, \tag{72}$$

$$K_{II}^{(1)} = \frac{1}{D_o \sqrt{S'_{11}}} M^{(1,2b)}, \tag{73}$$

$$K_{III}^{(1)} = \frac{1}{\sqrt{S'_{44} S'_{55} - S_{45}^2}} M^{(1,2c)}. \tag{74}$$

Of course, the appropriate asymptotic expressions for solutions (2a), (2b) and (2c) must be employed.

### 3.2. Displacement extrapolation method

Displacement extrapolation is the simplest method to implement; but it is the least accurate. In this study, it is employed as a check on the energy based methods. This method has been presented and implemented in many papers for isotropic materials.

For monoclinic materials, the displacement jump along the crack faces in the neighborhood of the crack tip is given by

$$\Delta u_1 = 2S'_{11} \sqrt{\frac{2r}{\pi}} [K_I \mathfrak{I}(p_1 p_2) + K_{II} \mathfrak{I}(p_1 + p_2)], \tag{75}$$

$$\Delta u_2 = -2S'_{22} \sqrt{\frac{2r}{\pi}} \left[ K_I \mathfrak{I}\left(\frac{p_1 + p_2}{p_1 p_2}\right) + K_{II} \mathfrak{I}\left(\frac{1}{p_1 p_2}\right) \right], \tag{76}$$

$$\Delta u_3 = 2K_{III} \sqrt{\frac{2r}{\pi}} \sqrt{S'_{44} S'_{55} - S_{45}^2}. \tag{77}$$

It may be noted that, similar to isotropic materials,  $\Delta u_i / \sqrt{r}$  along the crack faces is linear in  $r$  near the crack tip. Hence, the justification for linear displacement extrapolation (see [3] for details on isotropic materials).

With the displacement extrapolation method, the stress intensity factors are solved for in Eqs. (75)–(77). This leads to values of  $K$  which differ for each point along the crack faces. This variation of  $K$  is defined as  $K^*$  leading to

$$K_I^* = \frac{1}{4S'_{11} S'_{22} D_m} \sqrt{\frac{2\pi}{r}} \left[ \Delta u_1 S'_{22} \mathfrak{I}\left(\frac{1}{p_1 p_2}\right) + \Delta u_2 S'_{11} \mathfrak{I}(p_1 + p_2) \right], \tag{78}$$

$$K_{II}^* = -\frac{1}{4S'_{11} S'_{22} D_m} \sqrt{\frac{2\pi}{r}} \left[ \Delta u_1 S'_{22} \mathfrak{I}\left(\frac{p_1 + p_2}{p_1 p_2}\right) + \Delta u_2 S'_{11} \mathfrak{I}(p_1 p_2) \right], \tag{79}$$

$$K_{III}^* = \frac{1}{4\sqrt{S'_{44} S'_{55} - S_{45}^2}} \sqrt{\frac{2\pi}{r}} \Delta u_3, \tag{80}$$

where

$$D_m = \mathfrak{I}(p_1 p_2) \mathfrak{I}\left(\frac{1}{p_1 p_2}\right) - \mathfrak{I}(p_1 + p_2) \mathfrak{I}\left(\frac{p_1 + p_2}{p_1 p_2}\right). \tag{81}$$

As will be described in the section on results, values of  $K_j^*$  are plotted for points along the crack faces and fit with a ‘best’ line.

For orthotropic materials in which the material and crack coordinates coincide, the expressions in (78) and (79) become

$$K_I^* = \frac{\sqrt{2\pi}}{4} \frac{1}{\sqrt{S'_{22}D_o}} \frac{\Delta u_2}{\sqrt{r}}, \quad (82)$$

$$K_{II}^* = \frac{\sqrt{2\pi}}{4} \frac{1}{\sqrt{S'_{11}D_o}} \frac{\Delta u_1}{\sqrt{r}}, \quad (83)$$

where  $D_o$  is given in (44) and  $K_{III}^*$  is given in (80).

### 3.3. Separated $J$ -integrals

For mixed modes I and II in isotropic materials, the  $J$ -integral was separated into components  $J_I$  and  $J_{II}$  each of which corresponds to  $K_I$  and  $K_{II}$ , respectively, by Ishikawa et al. [8]. Details of their proof and additions made here for orthotropic material are presented in Appendix A.

Until now in this study, no distinction has been made between the energy release rate and the  $J$ -integral. The  $J$ -integral is given precisely by Eq. (39), whereas it is equal to the energy release rate  $\mathcal{G}$ . The latter may be obtained from the crack closure integral. It may be noted that if the crack closure integral is employed to determine  $\mathcal{G}_I$  and  $\mathcal{G}_{II}$  for orthotropic material in which the material and problem coordinates coincide, there is a separation of the energy into modes I and II, namely, Eq. (43) may be written as

$$\mathcal{G}_I = \frac{D_o}{2} \sqrt{S'_{22}} K_I^2, \quad (84)$$

$$\mathcal{G}_{II} = \frac{D_o}{2} \sqrt{S'_{11}} K_{II}^2. \quad (85)$$

Note that mode III is not discussed here.

Moreover, the  $J$ -integrals, written as area integrals, are given by

$$J_I = \int_A \left( \sigma_{ij}^I \frac{\partial u^I}{\partial x_1} - W_I \delta_{1j} \right) \frac{\partial q_1}{\partial x_j} dA, \quad (86)$$

$$J_{II} = \int_A \left( \sigma_{ij}^{II} \frac{\partial u^{II}}{\partial x_1} - W_{II} \delta_{1j} \right) \frac{\partial q_1}{\partial x_j} dA, \quad (87)$$

where  $A$  is the area shown in Fig. 2, the superscript I and II represent, respectively, symmetric and asymmetric fields found in Eqs. (A.4), (A.5), (A.8) and (A.9), and

$$W_I = \frac{1}{2} \sigma_{ij}^I \epsilon_{ij}^I, \quad (88)$$

$$W_{II} = \frac{1}{2} \sigma_{ij}^{II} \epsilon_{ij}^{II}. \quad (89)$$

Substituting the asymptotic symmetric and asymmetric fields into (86) and (87) or their equivalents before being converted to area integrals leads to

$$J_I = C_1^{(I)} K_I^2 + C_2^{(I)} K_I K_{II} + C_3^{(I)} K_{II}^2, \quad (90)$$

$$J_{II} = C_1^{(II)} K_I^2 + C_2^{(II)} K_I K_{II} + C_3^{(II)} K_{II}^2, \quad (91)$$

where the coefficients  $C_i^{(j)}$  are sums of integrals given in (A.23) and (A.24), as well as some of the compliance coefficients. It has not been possible to show analytically that  $C_2^{(I)}$ ,  $C_3^{(I)}$ ,  $C_1^{(II)}$  and  $C_2^{(II)}$  are zero. All numerical examples showed them to be at least nine orders of magnitude smaller than  $C_1^{(I)}$  and  $C_3^{(II)}$ . The

latter two were seen to be equal to the coefficients in Eqs. (84) and (85), respectively, or to validate, at least numerically, Eqs. (A.27) and (A.28).

Because of the mixed term in Eq. (42) for monoclinic material, the separation obtained for the orthotropic material is not possible. But this direction was considered in detail. The symmetry and asymmetry conditions implicit in Eqs. (A.4) and (A.5), for example, where the symmetric field is denoted by mode I and the asymmetric field is denoted by mode II, are not correct for monoclinic material. If one denotes the I field by A and the II field by B, Eqs. (A.1)–(A.11) may be written by replacing the appropriate superscripts. These are no longer symmetric and asymmetric fields; each is mixed. Because of the interaction between normal and shear, stresses and strains for monoclinic materials

$$\epsilon_{ij}^A \neq S_{ijkl} \sigma_{kl}^A, \tag{92}$$

$$\epsilon_{ij}^B \neq S_{ijkl} \sigma_{kl}^B. \tag{93}$$

Equalities in (92) and (93) are required in the proof of path independence. Without path independence, it is still possible to obtain additional integrals and continue development of this method. This direction was not pursued here.

#### 4. Numerical results for material with $x_3 = z = 0$ a symmetry plane

In this section, the three methods described in Section 3 are applied to materials for which the symmetry plane is  $x_3 = z = 0$ . Recall that the  $x$ -,  $y$ - and  $z$ -axes refer to the crack and the  $x_r$ -axes refer to the material. Solutions are sought for examples found in the literature, as well as new solutions. The finite element program ADINA [2] is employed. Eight noded isoparametric elements are used with square, quarter-point singular elements about the crack tip.

In order to examine path independence of the  $M$ -integral and the separated  $J$ -integrals, the paths used for the examples are shown in Fig. 3. Path 1 is found to produce less accurate results. Sometimes, path 2 also does not produce accurate results. Thus, the averages indicated in the tables are for paths 3, 4 and 5.

Most of the results are presented in normalized form as

$$\tilde{K}_j = \frac{K_j}{\sigma \sqrt{\pi a}}, \tag{94}$$

where  $j = I, II$ ,  $\sigma$  is the applied stress and  $a$  is crack length for an edge crack or half crack length for a central crack. Mode III is not considered in the calculations.

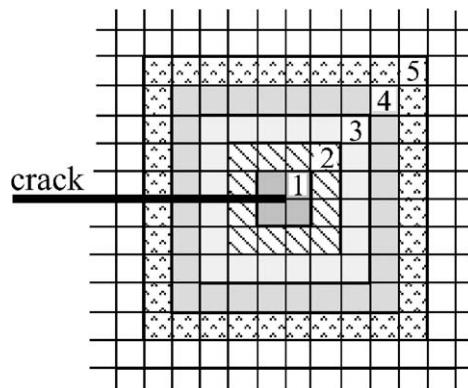


Fig. 3. Mesh and integration regions about the crack tip.

In Section 4.1, problems with solutions in the literature are examined for which the material is orthotropic such that material and crack coordinates coincide. In Section 4.2, similar problems are considered in which the material and crack coordinates are rotated with respect to each other. In this way, as a result of a transformation of the material compliance matrix from material coordinates to crack coordinates, the material appears monoclinic with respect to the crack. In Section 4.3, several new problems are solved.

#### 4.1. Linearly elastic, homogeneous, orthotropic material: comparison to solutions in the literature

Orthotropic material is defined by means of Young's moduli, Poisson's ratios and shear moduli. These parameters are related to the compliance coefficients as

$$\begin{aligned} S_{11} &= \frac{1}{E_{11}}, & S_{22} &= \frac{1}{E_{22}}, & S_{33} &= \frac{1}{E_{33}}, & S_{44} &= \frac{1}{\mu_{23}}, & S_{55} &= \frac{1}{\mu_{13}}, & S_{66} &= \frac{1}{\mu_{12}}, \\ S_{12} &= -\frac{\nu_{12}}{E_{11}} = -\frac{\nu_{21}}{E_{22}}, & S_{13} &= -\frac{\nu_{13}}{E_{11}} = -\frac{\nu_{31}}{E_{33}}, & S_{23} &= -\frac{\nu_{23}}{E_{22}} = -\frac{\nu_{32}}{E_{33}}. \end{aligned} \quad (95)$$

It should be noted that  $\nu_{ij} = -\epsilon_j/\epsilon_i$  when  $\sigma_i$  is the only applied stress.

##### 4.1.1. An infinite orthotropic body subjected to tension containing an angled crack

The first problem considered is an angled crack in an infinite orthotropic body subjected to tension as illustrated in Fig. 4. The material and problem coordinates coincide. This problem has an analytic solution which was obtained by Sih et al. [13] and is given by

$$K_I = \sigma\sqrt{\pi a} \sin^2\alpha, \quad (96)$$

$$K_{II} = \sigma\sqrt{\pi a} \sin\alpha \cos\alpha, \quad (97)$$

where  $\sigma$  is the applied far field stress,  $a$  is the half crack length and  $\alpha$  is the angle between the vertical and the crack.

In order to examine the three methods for calculating stress intensity factors, the crack angle  $\alpha = \pi/6$  is chosen. The normalized stress intensity factors from Eqs. (94), (96) and (97) are  $\tilde{K}_I = 0.2500$  and  $\tilde{K}_{II} = 0.4330$ . So that the body will be sufficiently large to simulate infinite conditions, the ratio 1:18.7 is chosen between the crack length  $2a$  and the height and width of the body. The material properties employed here are presented in Table 1 as Case 1. Both plane stress and plane strain conditions were assumed.

Three finite element meshes were constructed with different levels of refinement. These are exhibited in Fig. 5. Mesh 1 contains 552 elements and 1672 nodal points; mesh 2 contains 3324 elements and 10,061 nodal points; mesh 3 contains 13,156 elements and 39,564 nodal points. Only paths 1 and 2 in Fig. 3 exist

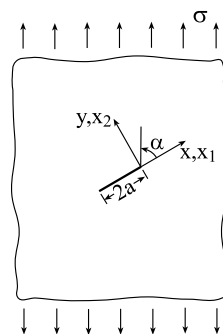


Fig. 4. Angled crack in an infinite orthotropic body.

Table 1  
Orthotropic mechanical properties employed for the geometry in Fig. 4

Case 1			Case 2		
$E_{11} = 10$	$E_{22} = 8$	$E_{33} = 6$	$E_{11} = 100$	$E_{22} = 2$	$E_{33} = 1$
$\nu_{12} = 0.1$	$\nu_{23} = 0.2$	$\nu_{13} = 0.3$	$\nu_{12} = 0.1$	$\nu_{23} = 0.2$	$\nu_{13} = 0.3$
$\mu_{12} = 4$	$\mu_{23} = 5$	$\mu_{13} = 6$	$\mu_{12} = 4$	$\mu_{23} = 5$	$\mu_{13} = 6$

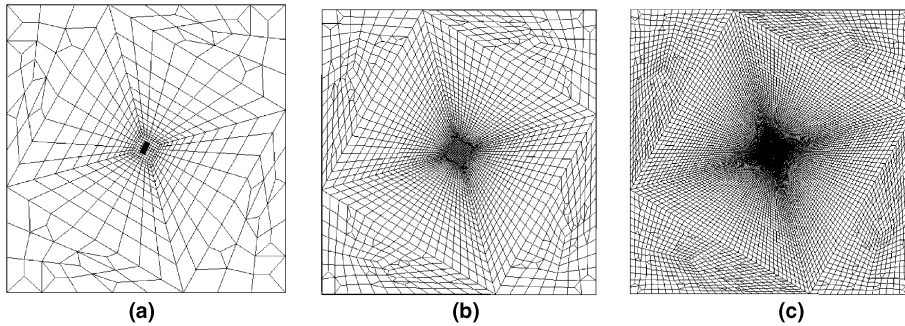


Fig. 5. Meshes constructed for the geometry in Fig. 4. (a) Mesh 1 contains 552 elements and 1672 nodal points (the crack is denoted as the solid line), (b) mesh 2 contains 3324 elements and 10,061 nodal points and (c) mesh 3 contains 13,156 elements and 39,564 nodal points.

for mesh 1. For meshes 1 and 2, the distance in the  $x$ -direction between the crack tip and the furthest path is the half crack length  $a$ ; for mesh 3 it is  $a/2$ .

Before employing the separated  $J$ -integrals in (86) and (87), calculations are made to obtain the coefficients  $C_i^{(j)}$  in (90) and (91). These cannot be computed once and for all, since they depend upon the eigenvalues  $p_i$ . They are obtained here by means of MAPLE [11]. The values which are expected to be zero, namely,  $C_2^{(I)}$ ,  $C_3^{(I)}$ ,  $C_1^{(II)}$  and  $C_2^{(II)}$  are found to be smaller than  $10^{-9}$ . The values of  $C_1^{(I)}$  and  $C_3^{(II)}$  agree with the coefficients in (84) and (85) to 10 significant figures and were  $O(10^{-1})$ . Calculations are carried out for both plane strain and plane stress conditions.

Both the separated  $J$ -integrals and the  $M$ -integral are employed along possible paths about the crack tip as shown in Fig. 3. For mesh 2 in Fig. 5, the stress intensity factors calculated along these paths are exhibited in Table 2. Except for the path within the quarter-point elements, the other paths yield the same values (except for path 2,  $K_{II}$  from the  $J_{MN}$ -integral). For this fine mesh, the lack of accuracy in the first path may be observed particularly for the  $M$ -integral.

Table 2  
Normalized stress intensity factors for the angled crack problem in Fig. 4 for crack angle  $\alpha = \pi/6$  and with material properties in Table 1 for Case 1

Path	$M$ -integral		$J_{MN}$ -integrals	
	$\tilde{K}_I$	$\tilde{K}_{II}$	$\tilde{K}_I$	$\tilde{K}_{II}$
1	0.2516	0.4343	0.2503	0.4320
2	0.2503	0.4334	0.2501	0.4330
3	0.2503	0.4334	0.2501	0.4331
4	0.2503	0.4334	0.2501	0.4331
5	0.2503	0.4334	0.2501	0.4331

Mesh 2 is used in the calculations.

Table 3

Normalized stress intensity factors for the angled crack problem in Fig. 4 with the crack angle  $\alpha = \pi/6$  and with material properties in Table 1 for Case 1

Mesh	$\tilde{K}_I$			$\tilde{K}_{II}$		
	$J_{MN}$	$M$	DE	$J_{MN}$	$M$	DE
1	0.2497	0.2502	0.2510	0.4327	0.4334	0.4506
2	0.2501	0.2503	0.2525	0.4331	0.4334	0.4389
3	0.2502	0.2503	0.2506	0.4333	0.4334	0.4334

Averages from paths 3 through 5 are exhibited in Table 3 for meshes 2 and 3. For mesh 1, path 2 is employed. In the table,  $J_{MN}$  refers to the values calculated with the separated  $J$ -integrals,  $M$  refers to the  $M$ -integral and DE specifies the displacement extrapolation method. It should be noted that the finite element results are obtained for plane strain conditions. Except for the first path in the elements adjacent to the crack tip, the results were nearly path independent. For  $J_{MN}$  the results from the first path differed by only 0.1% from the average results; for  $M$  the difference is 0.5%. Comparing to the exact solution, the energy based methods produce results which are in error of 0.1% or less.

The displacement extrapolation method is implemented, as well. This is not a particularly accurate method, but it produces results which may be employed as a check on the more exact results obtained by energy methods. In this study, the displacement jump across the crack faces is taken from the finite element results and substituted into Eqs. (82) and (83) to obtain  $K_I^*$  and  $K_{II}^*$ . These are plotted in a graph such as that in Fig. 6. Excluding the quarter point, a straight line is fit through three consecutive points near the crack tip and the correlation function  $R^2$  is calculated. The line with  $R^2$  closest to unity is chosen provided it is sufficiently near the crack tip. The intercept of this line with the ordinate provides the value of  $K$  which is exhibited in Table 3. The maximum difference between the stress intensity factors calculated by this method and the analytic solution is 4.1%.

In addition, for generalized plane stress conditions, the results were nearly the same and hence not exhibited.

It may be noted that the analytic results are for an infinite body. Thus, part of the slight difference between the values obtained here and the analytic values are a result of analysis of a large, but finite body. A larger body was analyzed with the crack length remaining the same. The results were closer to the analytic solution. If it is assumed that the results obtained for the finest mesh are the ‘best’ results for this size body, one may conclude that the  $M$ -integral converges even for the coarsest mesh as compared to the  $J_{MN}$ -integrals.

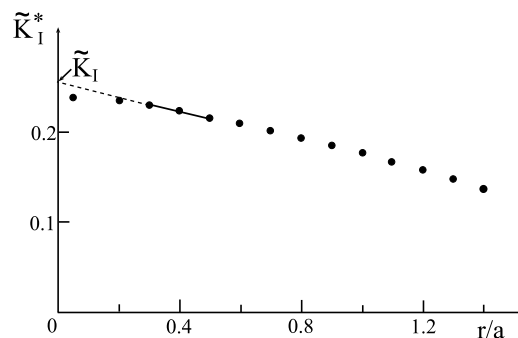


Fig. 6. The parameter  $\tilde{K}_I^*$  as a function of the distance from the crack tip along the crack faces for mesh 2 in Fig. 5b. The line shown is the one which produces the ‘best’ straight line.

Table 4

Normalized stress intensity factors for the angled crack problem in Fig. 4 with the crack angle  $\alpha = \pi/6$  and with material properties in Table 1 for Case 2

Path	$M$ -integral		$J_{MN}$ -integrals	
	$\tilde{K}_I$	$\tilde{K}_{II}$	$\tilde{K}_I$	$\tilde{K}_{II}$
1	0.2548	0.4117	0.2520	0.4152
2	0.2494	0.4377	0.2499	0.4317
3	0.2501	0.4334	0.2499	0.4317
4	0.2501	0.4329	0.2499	0.4317
5	0.2501	0.4328	0.2499	0.4316

Mesh 3 is used in the calculations.

For the mechanical properties shown in Table 1, the ratio  $E_{11}/E_{22} = 1.25$ , which is not very anisotropic. In order to examine the effect of a higher ratio,  $E_{11}/E_{22} = 50$  is chosen. The mechanical properties are presented in Table 1 as Case 2. The finest mesh in Fig. 5c is employed in the computations for  $J_{MN}$  and  $M$ . The displacement extrapolation method was not employed in this case.

Results for the stress intensity factors obtained by means of the two integral methods are presented in Table 4 for the five integration paths in Fig. 3. In reviewing the results, it is immediately apparent that the results obtained by  $J_{MN}$  are more stable than those obtained by  $M$ , in particular, for  $K_{II}$ . The average results for paths 3 through 5 is  $\tilde{K}_I = 0.2501$  and  $\tilde{K}_{II} = 0.4330$  for the  $M$  calculation; for  $J_{MN}$ , this average yields  $\tilde{K}_I = 0.2499$  and  $\tilde{K}_{II} = 0.4317$ . The greatest difference with the exact result is 0.3% for the latter value of  $\tilde{K}_{II}$ . This is in comparison to Case 1 in which the difference was  $-0.07\%$ . These differences together with the lack of path stability with the  $M$ -integral points to the difficulty in obtaining exact results when there is a high degree of anisotropy.

Thus, results from a still finer mesh are determined. This mesh, denoted as mesh 4, contains 24,516 elements and 73,524 nodal points. The region in which meshes 3 and 4 differ is exhibited in Fig. 7; this is the region surrounding the crack. For each element in the square surrounding the crack in Fig. 7a, there are four elements for mesh 4.

The results obtained for each of the meshes by means of the two energy based methods are presented in Table 5. In addition, to paths 1 through 5 defined in Fig. 3 there are two new paths: 6 and 7. In mesh 4, these paths are at a similar distance from the crack tip as paths 4 and 5 for mesh 3. The average values from paths 3 through 7 is  $\tilde{K}_I = 0.2501$  and  $\tilde{K}_{II} = 0.4333$  for the  $M$  calculation; for  $J_{MN}$ , this average yields  $\tilde{K}_I = 0.2500$  and  $\tilde{K}_{II} = 0.4325$ . It may be observed when considering four significant figures that identical

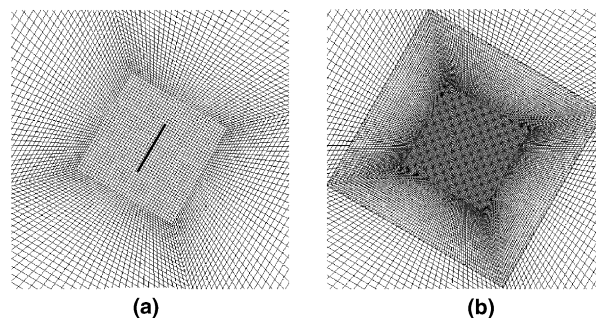


Fig. 7. Detail of meshes constructed for the geometry in Fig. 4. (a) Mesh 3 containing 13,156 elements and 39,564 nodal points for the entire mesh and (b) mesh 4 containing 24,516 elements and 73,524 nodal points.

Table 5

Normalized stress intensity factors for the angled crack problem in Fig. 4 with the crack angle  $\alpha = \pi/6$  and with material properties in Table 1 for Case 2

Path	<i>M</i> -integral		<i>J<sub>MN</sub></i> -integrals	
	$\tilde{K}_I$	$\tilde{K}_{II}$	$\tilde{K}_I$	$\tilde{K}_{II}$
1	0.2547	0.4111	0.2520	0.4147
2	0.2495	0.4381	0.2501	0.4328
3	0.2500	0.4337	0.2500	0.4327
4	0.2502	0.4330	0.2501	0.4323
5	0.2501	0.4334	0.2500	0.4326
6	0.2502	0.4331	0.2501	0.4325
7	0.2501	0.4331	0.2500	0.4325

Mesh 4 is used in the calculations.

results are not achieved for all paths especially for  $\tilde{K}_{II}$ . One might think that this lack of path independence reduces the reliability of the results. It may be pointed out, that path independence was achieved for the  $\tilde{K}_{II}$  values computed by means of the separated *J*-integrals with mesh 3 (see Table 3). But the solution did not converge to the correct value. Therefore, path independent results do not guarantee exactness. The mesh refinement carried out in mesh 4 did not improve significantly path stability; but the average results are closer to that of the infinite solution than the previous results for mesh 3.

It may be noted from the two material cases studied that there is an effect of the size of Young's moduli ratio on accuracy. The greater the deviation of this ratio from unity, the more difficult it is to attain accurate results.

#### 4.1.2. Finite orthotropic body containing a central crack subjected to tension

The next problem considered is shown in Fig. 8. It consists of a finite orthotropic body containing a central crack and subjected to tension. The material and crack axes coincide. This problem was solved by Bowie and Freese [6] by the boundary collocation method for a variety of material properties and geometric ratios. Conditions of plane stress were assumed. Bowie and Freese [6] defined the material properties through the eigenvalues of the compatibility equations  $p_1$  and  $p_2$ . They restricted their study to eigenvalues which are purely imaginary.

The geometric parameters are chosen here to be  $a/b = 1/2$  and  $h/b = 1$ . Two sets of material parameters are considered based upon given values of  $p_1$  and  $p_2$ ; these are presented in Table 6 as materials A and B. It may be noted that for problems in homogeneous anisotropic bodies, the stresses, as well as the stress intensity factors are functions of  $p_1$  and  $p_2$ . One can deduce this from expressions given in [16, pp. 129 and 420].

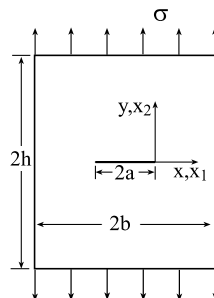


Fig. 8. Finite orthotropic body containing a central crack.

Table 6  
Orthotropic mechanical properties employed for the geometry in Fig. 8

Material	$\mathfrak{A}(p_1)$	$[\mathfrak{A}(p_2)]^2$	$E_{11}$	$E_{22}$	$\nu_{12}$	$\mu_{12}$
A	1	0.5	5	10	0.1	2.941
B	1	0.1	1	10	0.1	0.769

Determination of the mechanical properties yields an over-determined system of equations; so that two of the four material properties may be chosen arbitrarily. This leads to the mechanical properties shown in Table 6. These two sets of parameters are chosen to examine the effect of the ratio  $E_{11}/E_{22}$  on solution accuracy, path stability and convergence.

Beginning with material A, the solution presented by Bowie and Freese [6] is  $\tilde{K}_I = 1.46$ . Because of geometric, loading and material symmetry, it is possible to construct a mesh of one-quarter of the body. Since the post-processors developed here to calculate the stress intensity factors are for more general situations, meshes of one-half the body are constructed. To examine convergence, four meshes are employed. These are shown in Fig. 9. The integrals could be calculated on only two paths with mesh 1 which is rather coarse. For meshes 1 and 2 the distance between the crack tip and the furthest path along the  $x$ -axis is  $a$ ; whereas for meshes 3 and 4, this distance is respectively,  $a/5$  and  $a/10$ .

For the two integrals, near path independence is found for meshes 2 through 4, similar to that seen in Table 2 for the angle crack in an infinite body. There is a slight difference in the results obtained on a path within the quarter-point elements. In Table 7 results are presented which are obtained by means of the three methods. The paths chosen for presentation are path 2 for mesh 1 and the average of paths 3 through 5 for the other meshes. It may be noted that the results for these three paths yield identical results for each mesh. For the two energy methods, the result for the stress intensity factor converges to  $\tilde{K}_I = 1.455$  which when rounded to three significant figures agrees with the result of Bowie and Freese [6]. The boundary collocation method employed by Bowie and Freese [6] is known to yield rather accurate results. It may be noted that the convergence of the  $M$ -integral is slightly faster than the separated  $J$ -integrals. The results for meshes 3

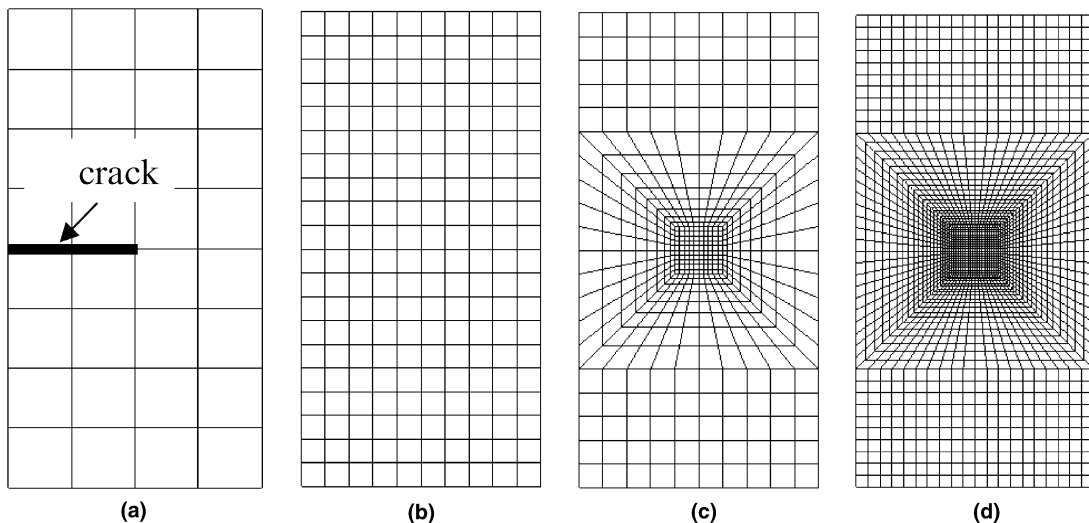


Fig. 9. Meshes constructed for the geometry in Fig. 8 with  $a/b = 1/2$  and  $h/b = 1$ . (a) Mesh 1 contains 32 elements and 125 nodal points, (b) mesh 2 contains 200 elements and 601 nodal points, (c) mesh 3 contains 520 elements and 1647 nodal points and (d) mesh 4 contains 2400 elements and 7381 nodal points.

Table 7

Normalized stress intensity factors for the problem in Fig. 8 with mechanical properties in Table 6 for materials A and B

Mesh	$\tilde{K}_I$ -case A			$\tilde{K}_I$ -case B		
	$J_{MN}$	$M$	DE	$J_{MN}$	$M$	DE
1	1.448	1.447	1.420	1.834	1.831	–
2	1.452	1.452	1.480	1.839	1.838	1.897
3	1.454	1.455	1.452	1.844	1.844	1.838
4	1.455	1.455	1.453	1.845	1.845	1.843

and 4 obtained by means of the displacement extrapolation method differ by less than about 1% from those of Bowie and Freese [6]. Those found with the coarser meshes are not as good.

For case B with the material parameters presented in Table 6 the result obtained by Bowie and Freese [6] is  $\tilde{K}_I = 1.85$ . Here the ratio  $E_{11}/E_{22} = 0.1$ . Path stability is slightly disturbed as compared to case A, more so for the  $J$ -integral. Results obtained for the same paths as in case A appear in Table 7 together with those obtained by means of the displacement extrapolation method. Values of  $\tilde{K}$  from the quarter-point element diverge from the average results. For mesh 4, for example, there is a difference of 0.9% for  $J$  and 1.4% for  $M$  with the solution of Bowie and Freese [6]. With the coarsest mesh, a result could not be obtained with the displacement extrapolation method for this material combination.

It may be concluded that it is more difficult to obtain path stability for  $E_{11}/E_{22}$  differing from unity. However, it is possible to obtain accurate results with sufficient mesh refinement. The first path through the quarter-point elements provides less accurate results, especially with the  $M$ -integral. Finally, it may be noted that displacement extrapolation produces  $K_{II} = 0$  exactly. For both materials, the conservative integrals provided values  $O(10^{-6})$  through  $O(10^{-15})$  for these values.

#### 4.2. Orthotropic material rotated with respect to crack axes: comparison to solutions in the literature

In Section 4.1, two geometries were considered for orthotropic material in which the material and crack axes coincided. In this section, two further problems are examined in which there is a difference between the material and crack axes. In the crack axes, the material appears monoclinic. In this case, the  $J_{MN}$ -integrals are not path independent. Hence, only the  $M$ -integral and displacement extrapolation method are employed. Here, the compliance coefficients in Eqs. (95) are calculated and then rotated to the crack coordinates.

The first problem considered is that of a crack rotated by an angle of  $\pi/4$  with respect to the horizontal axis. The body which is subjected to tension is sufficiently large compared to the crack length so that the results may be compared to an analytic solution for the infinite body. The second problem consists of a double edge cracked rectangular body subjected to tension. The material is orthotropic but rotated by an angle of  $\pi/4$  with respect to the crack axis.

##### 4.2.1. Orthotropic body subjected to tension containing a diagonal crack

An orthotropic rectangular plated subject to tension containing an angled crack is shown in Fig. 10. The material axes are in the  $x_1$ -,  $x_2$ -directions so that the crack axes are rotated by an angle of  $\alpha = \pi/4$  with respect to them. Atluri et al. [1] solved this problem employing the material properties presented in Table 8. Recall that in that study, a hybrid finite element approach was used with special singular elements at the crack tip and quadratic elements in the remainder of the body. The mesh included 96 elements and 260 nodal points. The geometric parameters used were  $b = 10$  in.,  $h = 20$  in.,  $a = \sqrt{2}$  in., and  $\sigma = 1$  psi. The results obtained by Atluri et al. [1] were  $K_I = 1.0195$  psi  $\sqrt{\text{in.}}$  and  $K_{II} = 1.0759$  psi  $\sqrt{\text{in.}}$

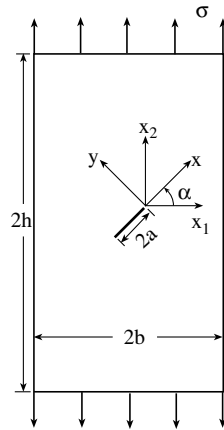


Fig. 10. Angled crack in a rectangular orthotropic body.

Table 8

Orthotropic mechanical properties with respect to the  $x_1$ -,  $x_2$ -axes, employed for the geometry in Fig. 10

$E_{11}$ (psi)	$E_{22}$ (psi)	$\mu_{12}$ (psi)	$\nu_{12}$
$3.5 \times 10^{-6}$	$12.0 \times 10^{-6}$	$3.0 \times 10^{-6}$	0.7

In order to examine convergence of the results, five finite element meshes are constructed which are illustrated in Fig. 11. Meshes 1 and 2 have the same refinement in the vicinity of the crack tip with a different total number of elements. Mesh 3 is further refined. Meshes 4 and 5 have the same refinement in the vicinity of the crack tip with mesh 5 containing substantially more elements. For the  $M$ -integral with meshes 1 through 3, the furthest path is a distance  $a$  from the crack tip along the  $x$ -axis. For meshes 4 and 5 this distance is reduced to  $a/2$ .

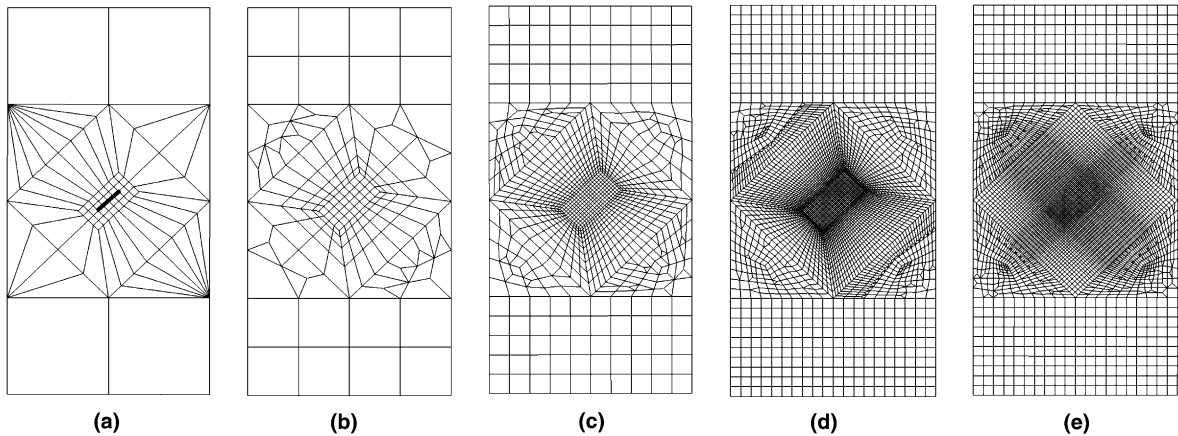


Fig. 11. Meshes constructed for the geometry in Fig. 10 with  $b/a = 5\sqrt{2}$  and  $h/b = 2$ . (a) Mesh 1 contains 84 elements and 248 nodal points, (b) mesh 2 contains 188 elements and 584 nodal points, (c) mesh 3 contains 1092 elements and 3220 nodal points, (d) mesh 4 contains 4336 elements and 13,096 nodal points and (e) mesh 5 contains 5986 elements and 17,914 nodal points.

Table 9

The stress intensity factors  $K_I$  and  $K_{II}$  for the angled crack problem in Fig. 10 with material properties in Table 8

Mesh	1	2	3	4	5
$K_I$ (psi $\sqrt{\text{in.}}$ )					
$M$	1.0492	1.0665	1.0678	1.0682	1.0682
DE	1.0368	1.0536	1.0761	1.0705	1.0653
$K_{II}$ (psi $\sqrt{\text{in.}}$ )					
$M$	1.0420	1.0607	1.0620	1.0623	1.0623
DE	1.0651	1.0767	1.0709	1.0597	1.0596

With meshes 3 through 5, there is essentially path independence for paths 2 through 5 shown in Fig. 3 for both  $K_I$  and  $K_{II}$ . There are discrepancies within the quarter-point elements (path 1); for example, for  $K_{II}$  the difference is about 1% for meshes 3, 4 and 5 and the rest of the paths. In Table 9, the  $K_I$  and  $K_{II}$  values obtained by means of the  $M$ -integral as an average from paths 3 through 5 for meshes 3 through 5 are presented. For meshes 1 and 2, the values from path 2 are presented. In addition, results are obtained by means of displacement extrapolation.

Although there is a great difference between the total number of elements in meshes 4 and 5, the same results are obtained by means of the  $M$ -integral. Recall that the meshes surrounding the crack tip are the same. With meshes 1 and 2, however, the results obtained by this method are different even though the meshes surrounding the crack are the same. It appears that with sufficiently fine meshes, the elements away from the crack region are less important. For meshes 4 and 5, the results obtained by means of the displacement extrapolation method differ by less than 0.3% with those obtained with the  $M$ -integral. However, there are multiple answers that may be chosen. In addition, results obtained with the path independent integral and mesh 2 are quite good.

The differences between the results found by Atluri et al. [1] and the converged results of meshes 4 and 5 obtained with the  $M$ -integral are  $-4.8\%$  for  $K_I$  and  $1.3\%$  for  $K_{II}$ . Atluri et al. [1] compared their results to an angled crack in an infinite body shown in Fig. 4. Substituting  $\alpha = \pi/4$  into Eqs. (96) and (97), one obtains  $K_I = K_{II} = 1.0539 \text{ psi } \sqrt{\text{in.}}$ .

To address these discrepancies, a square body with  $b = h = 20 \text{ in}$  and  $a = \sqrt{2} \text{ in}$  (refer to Fig. 10) is considered. A larger body would be required to more accurately model an infinite body; note that  $b/a = 7.1$ . A mesh based on that in Fig. 11d with 5136 elements and 15,536 nodal points is constructed. The stress intensity factors obtained by means of the  $M$ -integral are  $K_I = 1.0628 \text{ psi } \sqrt{\text{in.}}$  and  $K_{II} = 1.0603 \text{ psi } \sqrt{\text{in.}}$ . These results are essentially identical on paths 2 through 5. The difference between these results and the infinite solution are  $-0.8\%$  and  $-0.6\%$  for  $K_I$  and  $K_{II}$ , respectively. If the geometric parameters of the body were made larger with respect to crack length, the  $K$  values should approach the exact solution as was found in Section 4.1.1. Hence, the results found with the finer meshes appear to be more reliable than those found by Atluri et al. [1].

#### 4.2.2. Double edge cracked rectangular orthotropic body: material and crack axes differ by $45^\circ$

The next problem considered was examined first by Atluri et al. [1] and then by Boone et al. [5]. It is a double edge cracked rectangular orthotropic body subjected to tension as shown in Fig. 12. The dimensions of the body are  $h/b = 4$ . The material axes are rotated by an angle of  $\alpha = \pi/4$  with respect to the crack axes. The material properties employed are presented in Table 10. Note that  $E_{11}/E_{22} = 14.3$ . The material is orthotropic in the  $x_1, x_2$  frame. Plane stress conditions are enforced.

In both investigations, only graphical results were presented. Two crack lengths are studied here:  $a/b = 0.4$  and  $a/b = 0.8$ . Results obtained by the two references from the literature are presented in Table 11; the numerical values were obtained by inspection from the graphs. These two crack lengths are chosen

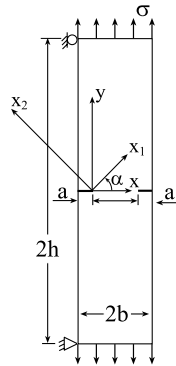


Fig. 12. Double edge cracked rectangular orthotropic body.

Table 10  
Orthotropic mechanical properties with respect to the  $x_1$ -,  $x_2$ -axes, employed for the geometry in Fig. 12

$E_{11}$ (psi)	$E_{22}$ (psi)	$\mu_{12}$ (psi)	$\nu_{12}$
$25 \times 10^6$	$1.75 \times 10^6$	$0.77 \times 10^6$	0.27

Table 11  
Results obtained from graphs presented by Atluri et al. [1] and Boone et al. [5] for the double edge cracked problem in Fig. 12 with material properties in Table 10

$alb$	Atluri et al. [1]		Boone et al. [5]	
	$\tilde{K}_I$	$K_{II}/K_I$	$\tilde{K}_I$	$K_{II}/K_I$
0.4	1.42	0.24	1.41	0.25
0.8	1.59	0.09	1.60	0.09

because of the excellent agreement between the two studies. Other results presented in those investigations did not agree as well. The method used by Atluri et al. [1] was described in the previous section. In that study, a mesh was constructed with 80 elements and 130 nodal points. Boone et al. [5] employed triangular quarter-point elements surrounding the crack tip and eight noded isoparametric elements elsewhere with an estimated total of 172 elements. The stress intensity factors were extracted by a displacement correlation method along the sides of the triangular elements on the crack faces.

Three meshes are employed here to determine the  $K$  values for  $alb = 0.4$ . The finest contains 6400 elements and 19,561 nodal points. The mesh surrounding the crack tips for this mesh is similar to that exhibited in Fig. 13a for  $alb = 0.8$ . Results calculated by means of the  $M$ -integral from this mesh are presented in Table 12. It may be noted that path independence is not quite as good as in previous examples. In addition, there is a difference for results obtained with this mesh and the path passing through the quarter-point elements of about  $-12\%$  for  $\tilde{K}_I$  and  $-36\%$  for  $K_{II}/K_I$ . For this problem, reliable results are not obtained from this path. Results from the displacement extrapolation method are not presented. Coarser meshes may be employed for this problem with similar results obtained. The ratio of  $E_{11}/E_{22}$  is the dominant factor influencing the quality of these results.

In the next geometry considered,  $alb = 0.8$ . The mesh employed for this crack length contains 6800 elements and 20,781 nodal points; that portion surrounding the crack tips is illustrated in Fig. 13a. Near path independence is achieved for paths 3 through 5. Results obtained from path 1 (through the quarter-point

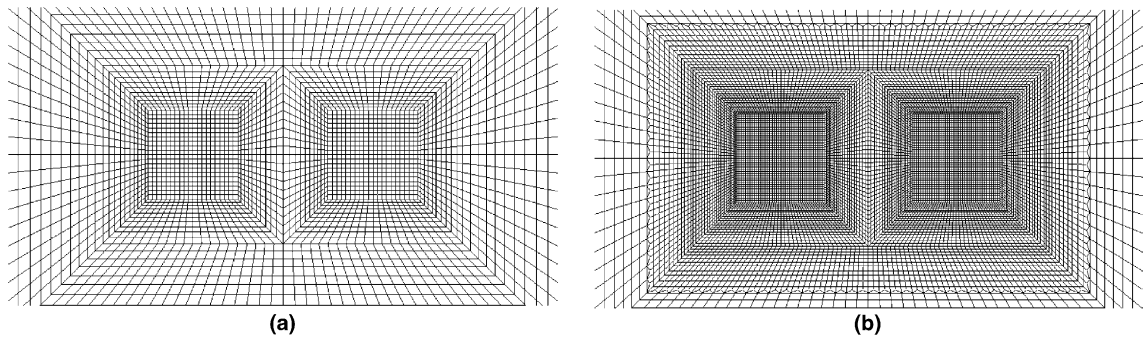


Fig. 13. Detail of meshes constructed for the geometry in Fig. 12. For  $alb = 0.8$ , total mesh contains for (a) 6800 and (b) 16,160 elements.

Table 12

Comparison of results obtained for the double edge cracked problem in Fig. 12 with material properties in Table 10

$alb$	$\tilde{K}_I$	% diff. A	% diff. B	$K_{II}/K_I$	% diff. A	% diff. B
0.4	1.410	0.7	0	0.239	0.4	4.4
0.8 (mesh, Fig. 13a)	1.678	-5.5	-4.9	0.0662	26.4	26.4
0.8 (mesh, Fig. 13b)	1.679	-5.6	-4.9	0.0667	25.9	25.9
0.8 (coarse mesh)	1.665	-4.7	-4.1	0.0923	2.6	2.6

A and B correspond respectively to results of Atluri et al. [1] and Boone et al. [5].

elements) differs by  $-10\%$  and  $-137\%$  for  $\tilde{K}_I$  and  $K_{II}/K_I$ , respectively, when compared to the average for paths 3 through 5. These differences appear to be caused by the large ratio of  $E_{11}/E_{22}$ , the proximity of the crack tips to one another and relative rotation of the crack plane to the orthotropic material directions. In spite of this, near path independence is achieved.

It may be noted that there are large differences between the results obtained in this study and those obtained by Atluri et al. [1] and Boone et al. [5] which nearly agree with each other. As a result of this poor agreement, a finer mesh is constructed containing 16,160 elements and 48,845 nodal points. The region surrounding the crack tips is exhibited in Fig. 13b. It may be noted that in this region, each element in the mesh in Fig. 13a has been divided into four elements. It is interesting to point out that the results from path 1 are essentially the same for both meshes. Those from path three for the finer mesh are in rather good agreement with those from the coarse mesh even though path 3 for the fine mesh is located in path 2 for the coarse mesh. It appears that most of the numerical noise caused by the singular stresses dies out by the third ring of elements regardless of element size. Two additional paths are added for the fine mesh and produce the same results as paths 3 through 5. The results for both meshes are quite similar.

The differences of the results with those of the two references is unsatisfactory. Hence, a mesh containing 690 elements with some refinement near the crack tips was constructed. These results are also presented in Table 12 as 'coarse mesh'. The result for  $K_{II}/K_I$  is much closer to that of the two references. Thus, a coarser mesh provides closer agreement with the results presented in the literature. The results obtained here with the very fine meshes and the  $M$ -integral are more accurate. It should be pointed out that at the time those studies were carried out, computers were much less capable.

#### 4.3. New solutions

In this section, problems involving actual materials are considered. One case is that of a cubic material characteristic of single crystal turbine blades used in some aircraft engines. The crack axis does not neces-

sarily coincide with the material axis. For most cases  $S'_{16} \neq S'_{26}$ . This problem is presented in Section 4.3.1. In Section 4.3.2, the problem of a through crack in the cortical bone of a femur is described. For both cases, the geometry and loading illustrated in Fig. 10 are studied with  $b/h = 1$  and  $a/h = 0.5$ . The  $x_1, x_2$  axes which relate to the material direction is constant as shown. The crack rotates with respect to the material direction.

To study convergence, four meshes are constructed for  $\alpha = \pi/12$  (see Fig. 10) which are shown in Fig. 14. As in the previous section, mesh 4 is obtained from mesh 3 with each element about the crack tips divided into four elements. Five other angles are also considered:  $\alpha = 0, \pi/6, \pi/4, \pi/3$  and  $5\pi/12$ . Convergence is not examined for the other angles and meshes with the same refinement in Fig. 14d are used. These meshes are illustrated in Fig. 15. For  $\alpha = 0$ , the same mesh shown in Fig. 9d is used. In this case, the material and crack axes coincide so that symmetry may be employed with a model of half the body. This mesh and the one in Fig. 14d have the same refinement about the crack tip.

#### 4.3.1. Cubic material: a single crystal superalloy

The material chosen here for study is used in jet engine turbine blades. It is a single crystal, nickel-based superalloy (PWA 1480/1493) described in a NASA report by Swanson and Arakere [15]. Its mechanical properties are given in Table 13. Plane strain conditions are enforced in the solution.

When the crack angle  $\alpha = 0$ , the crack and material axes coincide and it is possible to analyze the problem with all three methods ( $M$ -integral, separated  $J$ -integrals and the displacement extrapolation method). For  $\alpha = \pi/4$ ,  $S'_{16} = S'_{26} = 0$  so that again it is possible to use all three methods. For all other angles, the

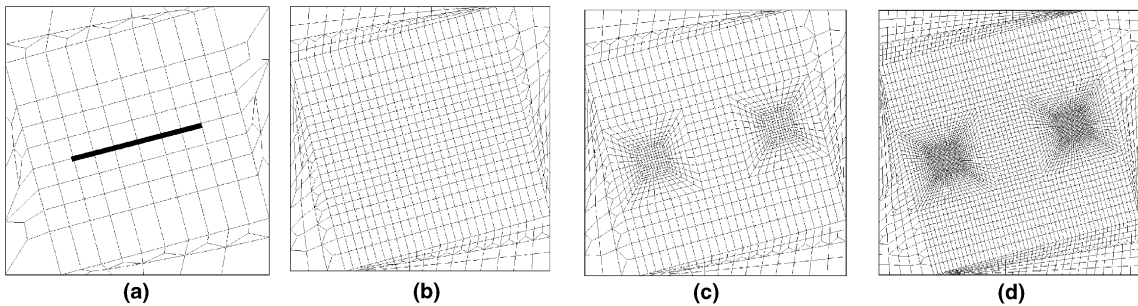


Fig. 14. Meshes constructed for the geometry in Fig. 10 for  $b/h = 1$ ,  $a/h = 0.5$  and  $\alpha = \pi/12$ . (a) Mesh 1 contains 142 elements and 454 nodal points, (b) mesh 2 contains 814 elements and 2498 nodal points, (c) mesh 3 contains 1374 elements and 4206 nodal points and (d) mesh 4 contains 5064 elements and 15,352 nodal points.

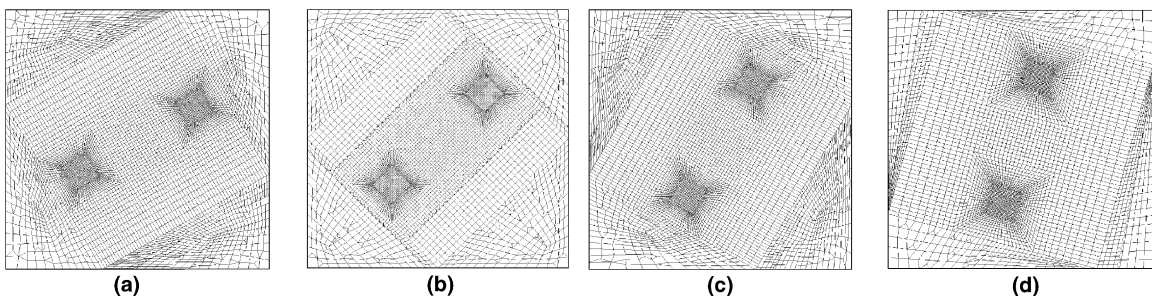


Fig. 15. Meshes constructed for the geometry in Fig. 10 for  $b/h = 1$  and  $a/h = 0.5$ . (a) For  $\alpha = \pi/6$ , the mesh contains 6070 elements and 18,290 nodal points; (b) for  $\alpha = \pi/4$ , the mesh contains 5804 elements and 17,456 nodal points; (c) for  $\alpha = \pi/3$ , the mesh contains 6070 elements and 18,290 nodal points; (d) for  $\alpha = 5\pi/12$ , the mesh contains 5064 elements and 15,352 nodal points.

Table 13

Cubic mechanical properties for PWA 1480/1493 employed for the geometry in Fig. 10 with  $b/h = 1$  and  $al/h = 0.5$ 

$$\begin{aligned}
 E_{11} = E_{22} = E_{33} &= 15.4 \times 10^6 \text{ (psi)} \\
 \mu_{12} = \mu_{23} = \mu_{13} &= 15.7 \times 10^6 \text{ (psi)} \\
 \nu_{12} = \nu_{23} = \nu_{13} &= 0.4009
 \end{aligned}$$

material appears to be monoclinic in the crack axes. In that case, only the  $M$ -integral and displacement extrapolation method may be used to calculate the stress intensity factors.

For both  $\alpha = 0$  and  $\pi/4$ , the constants in Eqs. (90) and (91) are sought. It is seen that  $C_1^{(I)}$  and  $C_3^{(II)}$  agree with the coefficients in Eqs. (84) and (85) to 10 and 9 significant figures for  $\alpha = 0$  and  $\pi/4$ , respectively. In the first case,  $C_2^{(I)}$ ,  $C_3^{(I)}$ ,  $C_1^{(II)}$  and  $C_2^{(II)}$  are 10 orders of magnitude smaller than the other coefficients. In the second case, it is reduced to eight orders of magnitude. Hence, the expressions in Eqs. (A.27) and (A.28) may be employed to calculate the stress intensity factors.

As mentioned, a convergence study for  $\alpha = \pi/12$  is carried out. Near path independence was observed for the  $M$ -integral along paths 2 through 5 (see Fig. 3) for both  $\tilde{K}_I$  and  $\tilde{K}_{II}$  for meshes 2 through 4. Mesh 1 provides only two integration paths. As usual, there are differences observed in the stress intensity factors along path 1 for each mesh. Results obtained by this method, as well as displacement extrapolation are presented in Table 14. Both methods appear to converge, although not to the same result. The difference for the finest mesh between results obtained by the two methods is 0.4% and 1.0% for  $\tilde{K}_I$  and  $\tilde{K}_{II}$ , respectively. With the coarsest mesh, these differences increase to  $-3.5\%$  and  $-1.1\%$ .

For other angles  $\alpha$ , the meshes in Figs. 9d and 15 have the same degree of refinement about the crack tips as that of mesh 4 in Fig. 14. For all angles, near path independence is achieved for the  $M$ -integral in paths 2 through 5. The largest difference between the value from the first path is  $-2.7\%$  for  $\alpha = 0$  and  $\tilde{K}_I$ . This difference examined with a finer mesh does not lead to any change of the results along the first path. For other angles, this difference was always less than 1%.

Boone et al. [5] showed that great errors may occur when calculating stress intensity factors for orthotropic materials in cases where the same geometry and mesh yield much more accurate results for isotropic material. For this cubic material, the relation between the shear modulus relative to the crack axes and that which would be calculated for an isotropic material are compared. To this end, in the crack axes, define  $E \equiv E'_{11} = E'_{22} = E'_{33}$ ,  $\mu \equiv \mu'_{12} = \mu'_{23} = \mu'_{13}$  and  $\nu \equiv \nu'_{12} = \nu'_{23} = \nu'_{13}$ . Let

$$X = \frac{E}{2(1 + \nu)} \quad (98)$$

which represents the shear modulus for an isotropic material. Comparison between  $\mu$  and  $X$  for the various crack angles is shown in Table 15. It may be observed that for the two values of  $\mu/X$  furthest from unity (2.9 and 0.35), the greatest errors in path 1 are obtained. Note that  $1/2.9 = 0.35$ . Thus, at the angles of  $\alpha = 0$  and  $\pi/4$  the worst results are obtained within the quarter-point elements. For all other cases, the same difference is obtained; 0.62 is the inverse of 1.6.

Table 14

Normalized stress intensity factors  $\tilde{K}_I$  and  $\tilde{K}_{II}$  for the angled crack problem in Fig. 10 with  $\alpha = \pi/12$  and material properties in Table 13

Mesh	$\tilde{K}_I$				$\tilde{K}_{II}$			
	1	2	3	4	1	2	3	4
$M$	1.2607	1.2667	1.2687	1.2692	0.2900	0.2908	0.2911	0.2912
DE	1.3053	1.2724	1.2645	1.2644	0.2932	0.2882	0.2883	0.2884

Table 15  
Mechanical properties in the crack coordinates for the geometry in Fig. 10 for various values of  $\alpha^a$

$\alpha$	$E (\times 10^6 \text{ psi})$	$\nu$	$\mu (\times 10^6 \text{ psi})$	$X (\times 10^6 \text{ psi})$	$\mu/X$	% diff.
0	15.4	0.40	15.7	5.5	2.9	−2.7
$\pi/12$	21.2	0.62	10.7	6.6	1.6	−0.3
$\pi/6$	30.9	0.44	6.6	10.7	0.62	0.3
$\pi/4$	40.1	0.28	5.5	15.7	0.35	0.6
$\pi/3$	30.9	0.44	6.6	10.7	0.62	0.3
$5\pi/12$	21.2	0.62	10.7	6.6	1.6	−0.3

<sup>a</sup> The mechanical properties in the  $x_1$ -,  $x_2$ -axes are given in Table 13. The percent difference for  $\tilde{K}_I$  is between path 1 and the averaged values from paths 3 through 5.

For both  $\alpha = 0$  and  $\pi/4$ , the  $J_{MN}$ -integrals are employed. Again, calculations are carried out along paths 1 through 5. Nearly identical results are obtained on paths 3 through 5. Differences between values from path 1 are less than 1%. In particular for  $\alpha = 0$ , the difference for  $\tilde{K}_I$  is −0.5%. Again it is observed that the  $J_{MN}$ -integrals produce better results in the singular elements.

A summary of results is presented in Table 16. These include averages of paths 3 through 5 for the  $M$ -integral and the  $J_{MN}$ -integrals (the latter for  $\alpha = 0$  and  $\pi/4$ ). It is possible to observe the excellent agreement between  $K$  values obtained by means of these two methods. This was also seen for results in Section 4.1 in which the material and crack coordinates coincided. For  $\alpha = 0$ ,  $\tilde{K}_{II}$  is shown as zero. For displacement extrapolation it is exactly zero. For the other two methods it is  $O(10^{-7})$  to  $O(10^{-8})$  along various paths. The results obtained by the displacement extrapolation method differ from those obtained by means of the  $M$ -integral by between 0.1% and 9%.

#### 4.3.2. Orthotropic material-cortical bone from the proximal femur

Cortical bone from the proximal femur is studied. It is known that bone is inhomogeneous and visco-elastic. These two aspects of its material behavior are neglected and it is treated as an orthotropic, linearly elastic, homogeneous material. Wirtz et al. [19] surveyed 300 experimental studies measuring material properties of this bone. Some typical properties are taken to be used in the analyses here. These are presented in Table 17. With these properties, only plane stress conditions may be imposed.

The same geometry studied in the previous section is considered with these material properties. It is clear that the proximal femur is a three-dimensional body including underlying cancellous bone in certain regions. This is a simplified model. As opposed to the cubic material studied, only when  $\alpha = 0$  can the separated  $J$ -integrals be employed. For all other angles, only the  $M$ -integral and displacement extrapolation method are used.

Table 16  
Normalized stress intensity factors  $\tilde{K}_I$  and  $\tilde{K}_{II}$  for the angled crack problem in Fig. 10 for various values of  $\alpha$  and material properties in Table 13

$\alpha$	0	$\pi/12$	$\pi/6$	$\pi/4$	$\pi/3$	$5\pi/12$
$\tilde{K}_I$						
$M$	1.3577	1.2692	1.0268	0.6952	0.3579	0.1095
$J_{MN}$	1.3576	–	–	0.6951	–	–
DE	1.3507	1.2644	1.0239	0.6926	0.3575	0.0994
$\tilde{K}_{II}$						
$M$	0	0.2912	0.5092	0.5807	0.5248	0.3108
$J_{MN}$	0	–	–	0.5806	–	–
DE	0	0.2884	0.5073	0.5935	0.5270	0.3105

Table 17

Orthotropic mechanical properties with respect to the  $x_1$ -,  $x_2$ -axes, employed for the geometry in Fig. 10 (see [19])

$E_{11}$ (MPa)	$E_{22}$ (MPa)	$\mu_{12}$ (MPa)	$\nu_{12}$
3.5	12.0	3.0	0.7

Table 18

Normalized stress intensity factors  $\tilde{K}_I$  and  $\tilde{K}_{II}$  for the angled crack problem in Fig. 10 for various values of  $\alpha$  and material properties in Table 17

$\alpha$	0	$\pi/12$	$\pi/6$	$\pi/4$	$\pi/3$	$5\pi/12$
$\tilde{K}_I$						
$M$	1.4349	1.3336	1.0577	0.6926	0.3434	0.0922
DE	1.4326	1.3335	1.0559	0.6913	0.3427	0.0920
$\tilde{K}_{II}$						
$M$	0	0.3310	0.5634	0.6306	0.5318	0.3036
DE	0	0.3302	0.5623	0.6300	0.5313	0.3030

Calculations are made for  $\alpha = \pi/12$  first to examine convergence. With meshes 1 through 4 in which calculations may be made along paths 1 through 5 with the  $M$ -integral, there is essentially path independence for both  $\tilde{K}_I$  and  $\tilde{K}_{II}$  except along the path through the quarter point elements. The maximum differences obtained between path 1 and the other paths is  $-0.2\%$  for  $\tilde{K}_I$  and  $-2\%$  for  $\tilde{K}_{II}$  for all the meshes. The values converge to  $\tilde{K}_I = 1.3336$  and  $\tilde{K}_{II} = 0.3310$  with mesh 4. The difference between the values obtained with this mesh and mesh 1 is  $0.4\%$  for both  $\tilde{K}_I$  and  $\tilde{K}_{II}$ . For mesh 4, results obtained with the displacement extrapolation method differed by at most  $0.2\%$  for both  $\tilde{K}_I$  and  $\tilde{K}_{II}$ . This should not mislead the reader to view the displacement extrapolation method as being of equal accuracy as that of the  $M$ -integral. There are many ways to choose the points for carrying out the linear regression. In addition, the mesh used here is overly fine. For this material, it is not difficult to obtain accurate results.

Results obtained by means of the  $M$ -integral and the meshes in Figs. 9d, 14d and 15 for  $\alpha = 0, \pi/12, \pi/6, \pi/4, \pi/3$  and  $5\pi/12$ , respectively, are exhibited in Table 18. These values are the same along paths 3 through 5. If there are differences along path 2, they are in the fifth significant figure. As previously, there are some differences in path 1. It may be noted that in contrast to the results obtained for the cubic material presented in the previous section, the difference between the result obtained along path 1 and that in Table 18 for  $\alpha = 0$  is  $-0.03\%$ . For  $\tilde{K}_I$ , the error in the results of path 1 increases for increasing  $\alpha$  with the greatest difference being  $-1.5\%$  for  $\alpha = 5\pi/12$ . The opposite behavior is observed for  $\tilde{K}_{II}$  with the difference  $-2\%$  for  $\alpha = \pi/6$  and decreasing to  $-0.2\%$  for  $\alpha = 5\pi/12$ . When  $\alpha = 0$ ,  $\tilde{K}_{II}$  is  $O(10^{-12})$  when calculated by the  $M$ -integral and  $O(10^{-10})$  with the  $J_{II}$ -integral.

In using the separated  $J$ -integrals the coefficients  $C_1^{(I)}$  and  $C_3^{(II)}$  in Eqs. (90) and (91) agree to 9 significant figures with the coefficients in Eqs. (A.27) and (A.28). These coefficients are  $O(10^{-10})$  whereas the others are negligible and of  $O(10^{-19})$ . Results obtained by this method are identical to those obtained by means of the  $M$ -integral and shown in Table 18; note that this method is only employed for  $\alpha = 0$ .

## 5. Summary and conclusions

In this study, the stress and displacement fields determined by Hoening [7] for a crack in a general anisotropic material are reviewed. Special anisotropies in which  $x_3 = z = 0$  is a symmetry plane are also considered. Recall that  $x, y$  and  $z$  are crack coordinates and  $x_1, x_2$  and  $x_3$  are material coordinates. For all cases,

the relationship between the *J*-integral and stress intensity factors was presented. Three methods were derived for calculating stress intensity factors for the special anisotropies. These include the *M*-integral, displacement extrapolation and the separated *J*-integrals. The first two are general and may be applied for all anisotropies. The latter may be applied for special symmetries, for example, when the material and crack coordinates coincide.

Four problems with solutions in the literature were studied. In the first two cases, the material and crack axes coincided. The greater the difference between the ratio  $E_{11}/E_{22}$  from unity, the more difficult it was to obtain accurate results. The best results were obtained with the *M*-integral. It is not necessary to use the finest meshes with this method to obtain accurate results, although sufficient mesh refinement about the crack tips is required. For a sufficiently refined mesh, the third ring about the crack tip, irrespective of element size, leads to accurate results. It appears that the major inaccuracies are within the ring containing the quarter point elements. The displacement extrapolation method produces results which differ by at most 5% for these problems from the comparative results. The *J*-integrals are limited to certain symmetries and are therefore less useful than the *M*-integral.

In Part II, a through crack at an arbitrary angle to the material coordinates in three dimensions will be studied. The *M*-integral will be extended to three dimensions for this situation. A cubic material will be studied in depth.

**Appendix A. On the separated *J*-integrals**

For isotropic and orthotropic materials with certain symmetries, the *J*-integral may be separated into two integrals, one consisting of symmetric quantities and the other of asymmetric quantities. This method was first described by Ishikawa et al. [8] for isotropic materials.

For the coordinate system shown in Fig. 1, the field quantities are separated into symmetric and asymmetric parts, namely

$$\sigma_{ij} = \sigma_{ij}^{(I)} + \sigma_{ij}^{(II)}, \tag{A.1}$$

$$\epsilon_{ij} = \epsilon_{ij}^{(I)} + \epsilon_{ij}^{(II)}, \tag{A.2}$$

$$u_i = u_i^{(I)} + u_i^{(II)}. \tag{A.3}$$

The stresses are defined as

$$\left\{ \begin{matrix} \sigma_{11}^{(I)}(x_1, x_2) \\ \sigma_{22}^{(I)}(x_1, x_2) \\ \sigma_{12}^{(I)}(x_1, x_2) \end{matrix} \right\} = \frac{1}{2} \left\{ \begin{matrix} \sigma_{11}(x_1, x_2) + \sigma_{11}(x_1, -x_2) \\ \sigma_{22}(x_1, x_2) + \sigma_{22}(x_1, -x_2) \\ \sigma_{12}(x_1, x_2) - \sigma_{12}(x_1, -x_2) \end{matrix} \right\}, \tag{A.4}$$

$$\left\{ \begin{matrix} \sigma_{11}^{(II)}(x_1, x_2) \\ \sigma_{22}^{(II)}(x_1, x_2) \\ \sigma_{12}^{(II)}(x_1, x_2) \end{matrix} \right\} = \frac{1}{2} \left\{ \begin{matrix} \sigma_{11}(x_1, x_2) - \sigma_{11}(x_1, -x_2) \\ \sigma_{22}(x_1, x_2) - \sigma_{22}(x_1, -x_2) \\ \sigma_{12}(x_1, x_2) + \sigma_{12}(x_1, -x_2) \end{matrix} \right\}, \tag{A.5}$$

so that

$$\left\{ \begin{matrix} \sigma_{11}^{(I)}(x_1, -x_2) \\ \sigma_{22}^{(I)}(x_1, -x_2) \\ \sigma_{12}^{(I)}(x_1, -x_2) \end{matrix} \right\} = \left\{ \begin{matrix} \sigma_{11}^{(I)}(x_1, x_2) \\ \sigma_{22}^{(I)}(x_1, x_2) \\ -\sigma_{12}^{(I)}(x_1, x_2) \end{matrix} \right\} \tag{A.6}$$

and

$$\begin{Bmatrix} \sigma_{11}^{(II)}(x_1, -x_2) \\ \sigma_{22}^{(II)}(x_1, -x_2) \\ \sigma_{12}^{(II)}(x_1, -x_2) \end{Bmatrix} = \begin{Bmatrix} -\sigma_{11}^{(II)}(x_1, x_2) \\ -\sigma_{22}^{(II)}(x_1, x_2) \\ \sigma_{12}^{(II)}(x_1, x_2) \end{Bmatrix}. \quad (\text{A.7})$$

The strains are defined similarly. The displacements are given by

$$\begin{Bmatrix} u_1^{(I)}(x_1, x_2) \\ u_2^{(I)}(x_1, x_2) \end{Bmatrix} = \frac{1}{2} \begin{Bmatrix} u_1(x_1, x_2) + u_1(x_1, -x_2) \\ u_2(x_1, x_2) - u_2(x_1, -x_2) \end{Bmatrix}, \quad (\text{A.8})$$

$$\begin{Bmatrix} u_1^{(II)}(x_1, x_2) \\ u_2^{(II)}(x_1, x_2) \end{Bmatrix} = \frac{1}{2} \begin{Bmatrix} u_1(x_1, x_2) - u_1(x_1, -x_2) \\ u_2(x_1, x_2) + u_2(x_1, -x_2) \end{Bmatrix}, \quad (\text{A.9})$$

so that

$$\begin{Bmatrix} u_1^{(I)}(x_1, -x_2) \\ u_2^{(I)}(x_1, -x_2) \end{Bmatrix} = \begin{Bmatrix} u_1^{(I)}(x_1, x_2) \\ -u_2^{(I)}(x_1, x_2) \end{Bmatrix}, \quad (\text{A.10})$$

$$\begin{Bmatrix} u_1^{(II)}(x_1, -x_2) \\ u_2^{(II)}(x_1, -x_2) \end{Bmatrix} = \begin{Bmatrix} -u_1^{(II)}(x_1, x_2) \\ u_2^{(II)}(x_1, x_2) \end{Bmatrix}. \quad (\text{A.11})$$

Substitution of (A.1)–(A.3) into the  $J$ -integral in (39) leads to

$$J = J_{I I} + J_{I II} + J_{II I} + J_{II II}, \quad (\text{A.12})$$

where

$$J_{MN} = \int_{\Gamma} \left( W_{MN} n_1 - T_i^{(M)} \frac{\partial u_i^{(N)}}{\partial x_1} \right) ds \quad (M, N = I, II) \quad (\text{A.13})$$

and the strain energy density is given by

$$W_{MN} = \frac{1}{2} \sigma_{ij}^{(M)} \epsilon_{ij}^{(N)}. \quad (\text{A.14})$$

One may show that

$$\frac{\partial W_{MN}}{\partial \epsilon_{ij}^N} = \sigma_{ij}^M \quad \text{if } M = N, \quad (\text{A.15})$$

$$\frac{\partial W_{MN}}{\partial \epsilon_{ij}^N} = \frac{1}{2} \sigma_{ij}^M \quad \text{if } M \neq N. \quad (\text{A.16})$$

With (A.15), it is possible to show that  $J_{MN}$  is independent of path when  $M = N$ . But because of (A.16),  $J_{MN}$  is not path independent for  $M \neq N$ . This was not noticed by Ishikawa et al. [8].

However, if a path symmetric with respect to the  $x_1$ -axis is taken, it is possible to show that

$$J_{MN} = 0 \quad \text{if } M \neq N. \quad (\text{A.17})$$

In addition, it is possible to show for both isotropic and orthotropic materials in which the material and crack axes coincide, that  $J_{I I}$  and  $J_{II II}$  are independent of path. Redefining these as  $J_I \equiv J_{I I}$  and  $J_{II} \equiv J_{II II}$ . Under these conditions,

$$J = J_I + J_{II} \tag{A.18}$$

and  $J_I$  and  $J_{II}$  may be calculated along any path, as long as mirror points about the crack occur in the body being analyzed.

Substituting the asymptotic stress, strain and displacement fields into (A.13) for isotropic material and  $M = N$  leads to

$$J_I = \mathcal{G}_I = \frac{K_I^2}{H}, \tag{A.19}$$

$$J_{II} = \mathcal{G}_{II} = \frac{K_{II}^2}{H}, \tag{A.20}$$

where  $H = E$  for generalized plane stress conditions and  $H = E/(1 - \nu^2)$  for plane strain. For orthotropic material the situation is more complicated. By substituting the asymptotic relations into (A.13) it is found that

$$J_I = C_1^{(I)} K_I^2 + C_2^{(I)} K_I K_{II} + C_3^{(I)} K_{II}^2, \tag{A.21}$$

$$J_{II} = C_1^{(II)} K_I^2 + C_2^{(II)} K_I K_{II} + C_3^{(II)} K_{II}^2, \tag{A.22}$$

where  $C_l^{(I)}$  and  $C_l^{(II)}$  ( $l = 1, 2, 3$ ) are combinations of integrals of the sought

$$\int_{-\pi}^{\pi} \sqrt{\frac{\cos \theta \pm p_i \sin \theta}{\cos \theta \pm p_j \sin \theta}} F_k^{(1)} d\theta, \quad k = 1, 2, \tag{A.23}$$

$$\int_{-\pi}^{\pi} \frac{-\sin \theta \pm p_i \cos \theta}{\sqrt{(\cos \theta \pm p_i \sin \theta)(\cos \theta \pm p_j \sin \theta)}} F_k^{(2)} d\theta, \quad k = 1, 2, 3, \tag{A.24}$$

and  $i, j = 1, 2, 4, 5$ . In the integrals in (A.23) and (A.24),

$$F_k^{(1)} = \begin{cases} \cos^2 \theta, & k = 1, \\ \sin \theta \cos \theta, & k = 2, \end{cases} \tag{A.25}$$

and

$$F_k^{(2)} = \begin{cases} 1, & k = 1, \\ \sin^2 \theta, & k = 2, \\ \sin \theta \cos \theta, & k = 3. \end{cases} \tag{A.26}$$

In (A.23) and (A.24),  $p_4 = \bar{p}_1$  and  $p_5 = \bar{p}_2$ . It was not possible to analytically evaluate the integrals in (A.23) and (A.24) with the program MAPLE [11]. Hence for each material set, these integrals are obtained numerically. In all materials considered in this study, it was found that  $C_2^{(I)}$ ,  $C_3^{(I)}$ ,  $C_1^{(II)}$  and  $C_2^{(II)}$  are at least nine orders of magnitude smaller than  $C_1^{(I)}$  and  $C_3^{(II)}$  so that they may be neglected and to very high accuracy it was found that

$$J_I = \mathcal{G}_I = \frac{D_o}{2} \sqrt{S'_{11}} K_I^2, \tag{A.27}$$

$$J_{II} = \mathcal{G}_{II} = \frac{D_o}{2} \sqrt{S'_{22}} K_{II}^2, \tag{A.28}$$

where  $D_o$  is given in (44).

## References

- [1] Atluri SN, Kobayashi AS, Nakagaki M. A finite-element program for fracture mechanics analysis of composite material. In: Sendeckyj GP, editor. *Fracture mechanics of composites*, ASTM-STP 593. American Society for Testing and Materials; 1975. p. 86–98.
- [2] Bathe KJ. *ADINA-automatic dynamic incremental nonlinear analysis*. Version 7.5.0. Adina, R&D, Inc., Watertown, 2001.
- [3] Banks-Sills L. Application of the finite element method to linear elastic fracture mechanics. *Appl Mech Rev* 1991;44:447–61.
- [4] Banks-Sills L, Sherman D. On the computation of stress intensity factors for three-dimensional geometries by means of the stiffness derivative and *J*-integral methods. *Int J Fract* 1992;53:1–20.
- [5] Boone TJ, Wawrzyniek PA, Ingraffea AR. Finite element modeling of fracture propagation in orthotropic materials. *Engng Fract Mech* 1987;26:185–201.
- [6] Bowie OL, Freese CD. Central crack in plane orthotropic rectangular sheet. *Int J Fract* 1972;8:49–58.
- [7] Hoenig A. Near-tip behavior of a crack in a plane anisotropic elastic body. *Engng Fract Mech* 1982;16:393–403.
- [8] Ishikawa H, Kitagawa H, Okamura H. *J*-integral of a mixed mode crack and its application. In: *Mechanical behavior of materials*, ICM 3, Cambridge, England, 1979. p. 447–55.
- [9] Lekhnitskii SG. *Theory of elasticity of an anisotropic body*. San Francisco: Holden-Day; 1950 [in Russian, 1963, in English, translated by Fern P].
- [10] Li FZ, Shih CF, Needleman A. A comparison of methods for calculating energy release rates. *Engng Fract Mech* 1985;21:405–21.
- [11] MAPLE 7, Release 7, Version 7, Maple, Inc., Waterloo, 2001.
- [12] Rice JR. A path independent integral and the approximate analysis of strain concentration by notches and cracks. *J Appl Mech* 1968;35:379–86.
- [13] Sih GC, Paris PC, Irwin GR. On cracks in rectilinearly anisotropic bodies. *Int J Fract Mech* 1965;1:189–302.
- [14] Sih GC, Liebowitz H. *Mathematical theories of brittle fracture*. In: Liebowitz H, editor. *Fracture, An Advanced Treatise*, vol. II. New York: Academic Press; 1968. p. 68–188.
- [15] Swanson G, Arakere NK. Effect of crystal orientation on the analysis of single-crystal, nickel-based turbine blade superalloys. NASA Technical Report, NASA/TP-2000-210074, 2000.
- [16] Ting TCT. *Anisotropic elasticity—theory and applications*. Oxford: Oxford University Press; 1996.
- [17] Tohgo K, Wang ASD, Chou T. A criterion for splitting crack initiation in unidirectional fiber-reinforced composites. *J Compos Mater* 1993;27:1054–76.
- [18] Wang SS, Yau JF, Corten HT. A mixed-mode crack analysis of rectilinear anisotropic solids using conservation laws of elasticity. *Int J Fract* 1980;16:247–59.
- [19] Wirtz DC, Schiffers N, Pandorf T, Radermacher K, Weichert D, Forst R. Critical evaluation of known bone material properties to realize anisotropic FE-simulation of proximal femur. *J Biomechan* 2000;33:1325–30.
- [20] Yau JF, Wang SS, Corten HT. A mixed-mode crack analysis of isotropic solids using conservation laws of elasticity. *J Appl Mech* 1980;47:335–41.